Torres Anthony Derek (Orcid ID: 0000-0002-0531-5883)
Keppel-Aleks Gretchen (Orcid ID: 0000-0003-2213-0044)
Doney Scott C. (Orcid ID: 0000-0002-3683-2437)
Luis Kelly (Orcid ID: 0000-0001-9975-3480)
Petri Christof (Orcid ID: 0000-0002-7010-5532)
Pollard David Frank (Orcid ID: 0000-0001-9923-2984)
Velazco Voltaire Almario (Orcid ID: 0000-0002-1376-438X)
Warneke Thorsten (Orcid ID: 0000-0001-5185-3415)
Wunch Debra (Orcid ID: 0000-0002-4924-0377)

A geostatistical framework for quantifying the imprint of mesoscale atmospheric transport on satellite trace gas retrievals

Anthony D. Torres[1], Gretchen Keppel-Aleks[1], Scott C. Doney[2,3], Michaela Fendrock[4], Kelly Luis[5], Martine De Mazière[6], Frank Hase[7], Christof Petri[8], David F. Pollard[9], Coleen M. Roehl[10], Ralf Sussmann[11], Voltaire A. Velazco[9], Thorsten Warneke[8], and Debra Wunch[12]

1 Climate and Space Sciences and Engineering, University of Michigan Ann Arbor, MI 48109 USA
2 Environmental Sciences, University of Virginia, Charlottesville, VA, 22904 USA
3 Marine Chemistry & Geochemistry, Woods Hole Oceanographic Institution, Woods Hole, MA, 02543 USA
4 Earth, Atmospheric, and Planetary Sciences, Massachusetts Institute of Technology, Cambridge, MA, 02142 USA
5 School for the Environment, University of Massachusetts Boston, Boston, MA, 02125 USA
6 Royal Belgian Institute for Space Aeronomy, Brussels, Belgium
7 Karlsruhe Institute of Technology, IMK-ASF, Karlsruhe, Germany
8 Institute of Environmental Physics, University of Bremen, Bremen, Germany
9 National Institute of Water and Atmospheric Research, Lauder, New Zealand
10 Geological and Planetary Sciences, California Institute of Technology, Pasadena, CA, 91125 USA
11 Karlsruhe Institute of Technology, IMK-IFU, Garmisch-Partenkirchen, Germany
12 Department of Physics, University of Toronto, Toronto, Canada

Corresponding Author: Anthony D. Torres (adtorres@umich.edu)

Key Points:

- We developed a framework to relate high-frequency spatial variations to transport-induced temporal fluctuations in atmospheric tracers
- We use geostatistical analysis to quantify the variance budget for X_{CO_2} and X_{H_2O} retrieved from NASA's OCO-2 satellite
- Accounting for random errors, systematic errors, and real geophysical coherence in remotely sensed trace gas observations may yield improved flux constraints

Abstract

NASA's Orbiting Carbon Observatory-2 (OCO-2) satellite provides observations of total column-averaged CO_2 mole fractions (X_{CO_2}) at high spatial resolution that may enable novel constraints on surface-atmosphere carbon fluxes. Atmospheric inverse modeling provides an approach to optimize surface fluxes at regional scales, but the accuracy of the fluxes from inversion frameworks depends on key inputs, including spatially and temporally dense CO_2 observations and reliable representations of atmospheric transport. Since X_{CO_2} observations are sensitive to both synoptic and mesoscale variations within the free troposphere, horizontal atmospheric transport imparts substantial variations in these data, and must be either resolved explicitly by the atmospheric transport model or accounted for within the error covariance budget provided to inverse frameworks. Here, we used geostatistical techniques to quantify the imprint of atmospheric transport in along-track OCO-2 soundings. We compare high-pass filtered (<250 km, spatial scales that primarily isolate mesoscale or finer scale variations) along-track spatial variability in X_{CO_2} and X_{H_2O} from OCO-2 tracks to temporal synoptic and mesoscale variability from ground-based X_{CO_2} and X_{H_2O} observed by nearby Total Carbon Column Observing Network (TCCON) sites. Mesoscale atmospheric transport is found to be the primary driver of along-track, high frequency variability for OCO-2 X_{H_2O}. For X_{CO_2}, both mesoscale transport variability and spatially coherent bias associated with other elements of the OCO-2 retrieval state vector are important drivers of the along-track variance budget.

Plain Language Summary

Numerous efforts have been made to quantify sources and sinks of atmospheric CO_2 at regional spatial scales. A common approach to infer these sources and sinks requires accurate representation of variability of CO_2 observations attributed to transport by weather systems. While numerical weather prediction models have a fairly reasonable representation of larger-scale weather systems, such as frontal systems, representation of smaller-scale features (<250 km), is less reliable. In this study, we find that the variability of total-column averaged CO_2 observations attributed to these fine-scale weather systems accounts for up to half of the variability attributed to local sources and sinks. Here, we provide a framework for quantifying the drivers of spatial variability of atmospheric trace gases rather than simply relying on numerical weather prediction models. We use this framework to quantify potential sources of errors in measurements of total-column averaged CO_2 and water vapor from NASA's Orbiting Carbon Observatory-2 (OCO-2) satellite.

1 Introduction

Knowledge of regional surface-atmosphere carbon dioxide (CO_2) fluxes are required to understand anthropogenic and climatic influences on the global carbon cycle. Despite longstanding research efforts to develop a robust budget for surface fluxes of CO_2 (Bolin and Keeling, 1963; Enting and Mansbridge, 1989; Tans et al., 1990; Keeling et al., 1996; Peters et al., 2005; Chevallier et al., 2010; Peylin et al., 2013; Basu et al., 2018), these studies diverge in their estimates of the geographic distribution of sources and sinks of CO_2 (Gurney et al., 2002; Baker et al., 2006; Stephens et al., 2007). For example, Gurney et al. (2002) found uncertainties in regional scale carbon fluxes were greater than 0.5 Gt C yr^{-1} across various inversion frameworks. In these studies, carbon fluxes are inferred from spatial and temporal variations in atmospheric CO_2 observations via atmospheric inverse methods. Atmospheric inversions typically apply Bayesian optimal estimation methods to optimize assumed (a priori) fluxes that have been used as boundary conditions to simulate spatiotemporal CO_2 variations in an atmospheric transport model. Mismatches between the simulated and observed atmospheric CO_2 provide the basis for scaling the assumed fluxes. The optimization requires rigorous attention to errors associated with the assumed flux structure, the observations, and the fidelity of atmospheric transport modeled by the framework (Rogers, 2000).

One limitation to inverse modeling studies has been the density and geographic distribution of atmospheric observations available to constrain surface fluxes (Gurney et al., 2002). Traditionally, observations of atmospheric CO_2 have been measured in situ or via flask sampling within the atmospheric boundary layer. These observatories are concentrated within Northern Hemisphere temperate latitudes, and there is a scarcity of observations in key regions for the global carbon cycle, including the tropics (Stephens et al., 2007) and the Southern Ocean (Landschützer et al, 2015). The sparse in situ network for atmospheric CO_2 observations was the impetus for the launch of several satellites, including Japan Aerospace Exploration Agency's (JAXA) Greenhouse gases Observing SATellite (GOSAT) (Yokota et al, 2009; Ross et al., 2013), NASA's Orbiting Carbon Observatory-2 satellite (OCO-2) (Crisp et al., 2004; Eldering et al., 2017), and Chinese National Space Administration's (CNSA) TanSat (Yang et al., 2018). These low Earth, polar-orbiting satellites measure the total column averaged dry air mole fraction of atmospheric CO_2 (denoted as X_{CO_2}) at high spatial density. For example, OCO-2 acquires approximately 1 million soundings every day, each

with a footprint on the order of 1 km² (Crisp et al., 2004; Eldering et al., 2017). Theoretical studies have hypothesized that the high spatiotemporal density of X_{CO_2} observations may allow for a reduction of errors in flux inferences from inversion models (Rayner and O'Brien, 2001; Baker et al, 2006; Miller et al., 2007).

A second limitation to the fidelity of inverse modeling studies is the inverse modeling framework itself, via either incorrect parameterization of atmospheric transport (Masarie et al., 2011; Williams et al., 2014; Chevallier et al., 2010; Houwelling et al., 2015; Basu et al., 2018) or inappropriate representation of error covariance structures (Chevallier and O'Dell, 2013). The goal of this paper is to discuss the unique requirements for atmospheric transport fidelity and the description of variance budgets for X_{CO_2} from the OCO-2 satellite. One advantage of measuring the column averaged mole fraction is that its variations can be used more effectively to constrain surface fluxes via mass balance. Measurements made within the planetary boundary layer are sensitive not only to fluxes at the surface, but also to the rate at which the surface flux signal is entrained into the free troposphere. The column, however, is unaffected by the vertical entrainment rate, so in theory it is more directly related to surface fluxes via mass balance (Rayner and O'Brien, 2001; Olsen and Randerson, 2004). For example, Basu et al. (2018) concluded that fluxes inferred from perfect, or error-free, satellite observations of X_{CO_2} are less sensitive to uncertainty in atmospheric transport than perfect in situ observations of CO_2 in the planetary boundary layer by applying flux inversion techniques to the output from different atmospheric transport models forced with the same CO_2 initial and boundary conditions.

A potential complication of using X_{CO_2}, however, is that it is sensitive to CO_2 within the free troposphere, where most weather occurs. The variance budget is therefore strongly affected by horizontal advection (Geels et al., 2004; Keppel-Aleks et al., 2011), not just surface fluxes, which are the real target of obtaining and inverting atmospheric observations. In fact, at subseasonal timescales, horizontal advection dominates the variance budget in X_{CO_2} (Keppel-Aleks et al., 2011). Keppel-Aleks et al. (2012) used ground-based observations of X_{CO_2} at several midlatitude sites in the Total Carbon Column Observing Network (TCCON) to show that synoptic-scale variations, which occur on spatial scales on the order of 1000 km and temporal scales of about one to two weeks, could be up to half the peak-to-trough seasonal cycle in X_{CO_2}. Likewise, horizontal advection drives up to 60 to 70% of diurnal

variations of boundary layer CO_2 in the midlatitudes (Parazoo et al., 2008), and these horizontal eddy-induced variations are roughly half the size of the seasonal CO_2 variations driven by regional net ecosystem exchange of X_{CO_2}(Parazoo et al., 2011). At finer spatial scales on the order of 100 km, mesoscale variability in X_{CO_2}, which occurs on timescales of around one day, can be larger than diurnal variations in X_{CO_2} resulting from CO_2 exchange with the local terrestrial ecosystem (Keppel-Aleks et al., 2012). Mesoscale transport imposes especially large errors on flux inversions over cities at time scales smaller than a month (Lauvaux et al, 2016). However, even with global scale inversions, the variations on X_{CO_2} imparted by fine scale transport may ultimately degrade the inverted fluxes. This is largely due to the fact that signal imposed by fine and large-scale atmospheric transport is spatially correlated, thus these variations cannot simply be addressed simply by averaging multiple observations (Miller et al, 2015).

Thus, efforts to use X_{CO_2} from OCO-2 for flux inference must reliably account for transport-induced time/space variations, either through explicit simulation within the atmospheric transport model or by representation of transport-induced errors within the error covariance matrix. We note that larger-scale synoptic weather systems are more likely to be simulated explicitly by atmospheric inverse modeling frameworks, which generally have horizontal resolutions between 0.5° to 5° (Corbin et al., 2008), whereas mesoscale systems occur at spatial scales smaller than the grid-cell resolution for all but the highest resolution atmospheric transport models. These smaller mesoscale systems, therefore, may not be represented explicitly by atmospheric transport models despite affecting the distribution of X_{CO_2}. Because mesoscale or frontal systems may also have clouds, which obscure space-based X_{CO_2} measurements, it is important to quantify the variance and spatial coherence of X_{CO_2} that will be averaged from satellite measurements before for comparison with a single model grid-cell value (Corbin et al., 2008).

In this study, we use complementary information from space-based (OCO-2) and ground-based (TCCON) remote sensing of X_{CO_2} to quantify the imprint of mesoscale atmospheric transport and to refine the variance budget of OCO-2 X_{CO_2}. While the current suite of carbon observing satellites provide spatially dense observations, the time in between satellite overpasses at a specific location is too long (16 days for OCO-2) to sample temporal variations of X_{CO_2} driven by mesoscale (i.e., the duration of a thunderstorm) or synoptic-scale

systems (i.e., the time in between frontal systems, which is typically on the order of a week in mid latitude regions). In contrast, ground-based networks, such as TCCON, provide temporally dense, but spatially sparse observations. To use these observations together, we must develop a framework that relates the spatial variations in OCO-2 data to the temporal variations in TCCON data.

Throughout our analysis, we are cognizant of the fact that observing system error may also introduce variance to satellite data (Baker et al., 2010; Chevallier et al., 2014). For example, Worden et al. (2017) showed that natural variability (i.e., variations due to natural surface fluxes, anthropogenic emissions, and atmospheric transport) of X_{CO_2} along simulated representative OCO-2 tracks was negligibly small (approximately 0.08 ppm over 100 km neighborhoods) in comparison to variations of 1.28 ppm per 100 km attributed to instrument noise and slow varying biases, such as those caused by surface pressure or albedo variations, observed in OCO-2 data. Therefore, while the primary purpose of this study is to understand synoptic and mesoscale variations of X_{CO_2}, we also leverage retrievals of total column-averaged mole fractions of water vapor (X_{H_2O}) from OCO-2 (Nelson et al., 2016) and TCCON observations to validate our approach to estimating terms in Equation 5. Retrievals of water vapor from OCO-2 have a high signal-to-noise ratio (from several hundred to greater than 1000) (Nelson et al., 2016). Therefore, we expect that synoptic and mesoscale variations of atmospheric transport X_{H_2O} are more readily quantifiable from space-based observations.

This manuscript is organized around answering the following science questions.

  1.) What is the imprint of synoptic and mesoscale systems on X_{CO_2} (and X_{H_2O})?

  2.) How predictive are large-scale spatial gradients in X_{CO_2} (or X_{H_2O}) of the imprint of synoptic and mesoscale atmospheric transport on OCO-2 observations?

  3.) How large are other sources of fine-scale variation in X_{CO_2} (and X_{H_2O}) in the OCO-2 variance budget?

In Section 2, we describe the methods and framework we used to quantify variability attributed to synoptic and mesoscale atmospheric transport from both TCCON and along-track OCO-2 observations of X_{CO_2} and X_{H_2O}. In Section 3, we describe the variance budgets for OCO-2 X_{CO_2} and X_{H_2O} in the context of validation data from TCCON. In Section 4, we

provide discussion and recommendations for future work toward robust flux influence from the satellite data.

2 Methods

2.1 Framework to compare temporal and spatial variability of trace gases

This framework provides the basis to which we compare temporal mesoscale variability of along-track X_{CO_2} and X_{H_2O} observed at TCCON ground sites to along-track spatial mesoscale variability from OCO-2 data. We define along-track mesoscale spatial variability of X_{CO_2} and X_{H_2O} for tracks that occur within a 10° by 10° box of TCCON sites (Fig. 1). The domains of analysis chosen were large enough to encompass several representative atmospheric transport model grid cells, such as the 3° by 2° grid cells used by Basu et al. (2018) to infer carbon fluxes.
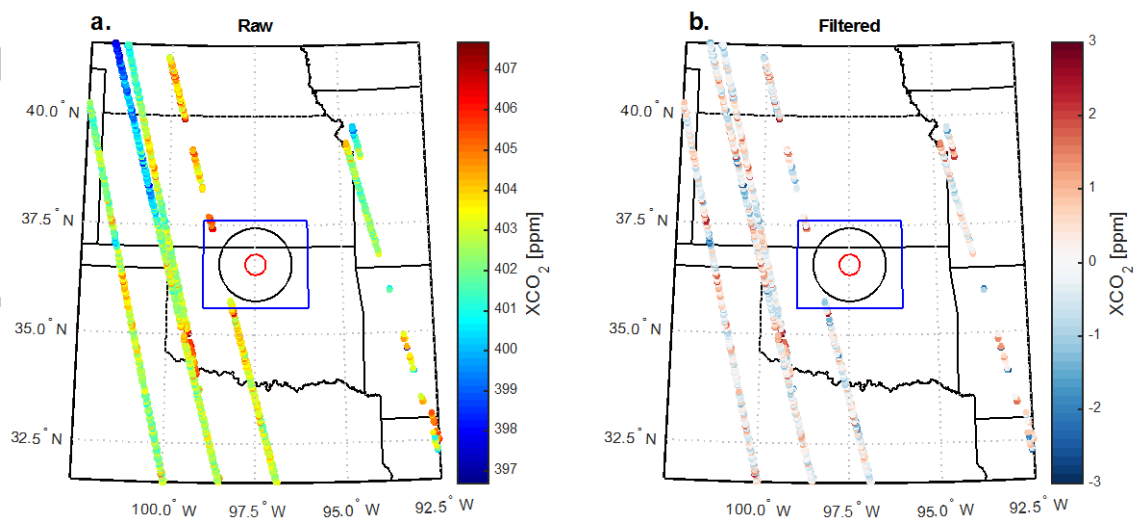
Figure 1. X_{CO_2} tracks over a 10° × 10° domain centered on Lamont, Oklahoma for one 16-day repeat cycle in early July 2016. (**a.**) Raw XCO2 soundings and (**b.**) High-pass filtered X_{CO_2}. The radius of the red and black circle represents the monthly mean range (denoted as a_{space}) of explained variability of X_{CO_2} and X_{H_2O}, respectively in July. The blue box represents a typical 3° × 2° grid cell used in atmospheric inversion models, such as those used in Basu et al. (2018).

We start from the tracer conservation equation in one dimension:

$$\frac{\partial c}{\partial t} = -u\frac{\partial c}{\partial x} + S_c \text{ (Equation 1)}$$

where c represents the tracer concentration, in this case X_{CO_2}, u represents the column-weighted wind velocity in one direction (assumed along the OCO-2 track), and S_c represents the column-average surface sources and sinks of CO_2 (with appropriate scaling to convert from flux to X_{CO_2} column-average variation). In this equation, we have neglected molecular diffusion of X_{CO_2}, which is small relative to the other terms, and any variations in u and CO_2 in the vertical profile by simply using the total column averages. We decompose c into its mean and variable components (Equation 2)

$$c = \overline{c} + c' \text{ (Equation 2)}$$

and Reynolds average Equation 1 to yield an equation for the time rate of change of $\overline{c}$ (Equation 3). For our analysis, we assume that the filter used to determine the average concentration, $\overline{c}$, results in a c' that reflects mesoscale variations in the tracer concentration while synoptic and slower- and larger-scale variations remain in $\overline{c}$.

$$\frac{\partial \overline{c}}{\partial t} = -\overline{u}\frac{\partial \overline{c}}{\partial x} - \frac{\partial \overline{u'c'}}{\partial x} + \overline{S}_c \text{ (Equation 3)}$$

The first term on the right hand side represents the advection of the mean gradient in c by the mean wind, while the second term represents turbulent flux divergence. Equation 3 underscores that spatial gradients in the mean tracer concentration give rise to temporal variations through the action of atmospheric transport. We can subtract equation 3 from equation 1, expanded by replacing u and c with the corresponding mean and anomaly terms from equation 2 (and equivalent equation for u), to yield an equation for the time rate of change for the fluctuating component, c':

$$\frac{\partial c'}{\partial t} = -\overline{u}\frac{\partial c'}{\partial x} - u'\frac{\partial \overline{c}}{\partial x} - u'\frac{\partial c'}{\partial x} + \frac{\partial \overline{u'c'}}{\partial x} + S'_c \text{ (Equation 4)}$$

In equation 4, the first term on the right hand side represents the advection of mesoscale gradients by the mean wind, the second term and third terms represent the production of mesoscale anomalies in c by eddies acting on the mean gradient and mesoscale gradient,

respectively. The fourth term represents the turbulent flux convergence. We can simplify equation 4 by assuming that the production term from eddies acting on mesoscale gradients and the turbulent flux convergence are both small. We also neglect variations in sources, S'_c, since our framework accounts for only climatological mean surface fluxes (described in detail in 3.2.1 below). We can then use scaling arguments to approximate these terms:

$$\frac{\langle c' \rangle_{time}}{\tau_{time}} = \overline{u} \frac{\langle c' \rangle_{space}}{a_{space}} + \langle u' \rangle \langle \frac{\partial \overline{c}}{\partial x} \rangle \text{ (Equation 5)}$$

In equation 5, $\langle c' \rangle_{time}$ represents the characteristic magnitude of temporal variations at a TCCON site over a relevant mesoscale timescale τ_{time}. The variable $\langle c' \rangle_{space}$ represents the characteristic magnitude of along-track spatial variations from OCO-2 over a relevant mesoscale length scale, a_{space}. The last term on the right-hand side (RHS) represents the advection of the mean gradient $\langle \frac{\partial \overline{c}}{\partial x} \rangle$ by mesoscale transport $\langle u' \rangle$.

The crux of our analysis is to compare $\langle c' \rangle_{time}$ and τ_{time} inferred from empirical analysis of TCCON observations with $\langle c' \rangle_{space}$ and a_{space} inferred from geostatistical analysis of high-pass filtered OCO-2 tracks. This analysis is conducted with an eye toward using the OCO-2 derived estimates of $\langle c' \rangle_{space}$ and a_{space} to improve the representation of fine scale transport errors within the error covariance budget provided to inverse models used for flux inference.

2.1 TCCON

We quantified temporal synoptic and mesoscale variations in X_{CO_2} and X_{H_2O} using ground-based remote sensing data from sites in the TCCON network (Table 1). TCCON sites are instrumented with ground-based Fourier Transform Spectrometers that acquire direct solar absorption spectra approximately every two minutes during sunny conditions (Wunch et al., 2015). TCCON instruments obtain near infrared spectra in the same spectral region as OCO-2 ($0.65 - 2.63$ μm), and total column CO_2 is retrieved in the 1.58 and 1.60 μm absorption bands and total column H_2O is retrieved in the $1.54 - 1.65$ μm absorption bands using the GFIT algorithm (Wunch et al., 2011). Because TCCON measures direct solar absorption spectra, the signal to noise ratio is higher compared to that of OCO-2, and the uncertainties on TCCON X_{CO_2} have a calibration accuracy of 0.4 ppm (Wunch et al., 2010). TCCON data are calibrated to the World Meteorological Organization (WMO) standard ensuring absolute accuracy of measurements better than 0.25% (Washenfelder et al., 2006; Wunch et al., 2011).

We analyzed data from TCCON sites that have data records longer than 5 years and that observe across a full annual cycle to minimize biases introduced by seasonal and interannual variations.

Table 1. Locations of TCCON sites and observational periods analyzed in this study with associated references.

TCCON Site	Location	Observational Periods	Citation
Bialystok, Poland	53.33°N, 23.03°E	March 13, 2009 – April 14, 2017	Deustcher et al. (2014)
Karlsruhe, Germany	49.10°N, 8.44°E	April 19, 2010 – January 24, 2018	Hase et al. (2014)
Orleans, France	47.97°N, 2.11°E	August 29, 2009 – April 29, 2017	Warneke et al. (2014)
Garmisch, Germany	47.48°N, 11.06°E	July 16, 2007 – March 16, 2018	Sussman and Rettinger (2014)
Park Falls, Wisconsin	45.95°N, 90.27°E	June 2, 2004 – December 31, 2017	Wennberg et al. (2014a), Washenfelder et al. (2006)
Lamont, Oklahoma	36.60°N, 97.49°W	July 6, 2008 – December 31, 2017	Wennberg et al. (2014b)
Darwin, Australia	12.42°S, 130.89°E	August 28, 2005 – March 28, 2017	Griffith et al. (2014), Deutscher et al., (2010)
Reunion Island, France	20.90°S, 55.49°E	September 16, 2011 – January 30, 2018	De Mazière et al. (2014)
Lauder, New Zealand	45.04°S, 169.69°E	February 2, 2010 – November 1, 2017	Sherlock et al. (2014)

2.1.1 Removing diurnal cycle climatology of X_{H_2O} and X_{CO_2} to quantify temporal synoptic and mesoscale variability

We separated the imprint of synoptic and mesoscale systems on variations in TCCON X_{CO_2} and X_{H_2O} by assuming that the only sources of variations were surface fluxes or atmospheric transport. For both X_{CO_2} and X_{H_2O}, we assumed that flux-driven diurnal variations could be accounted for by calculating a monthly climatological daily cycle of X_{CO_2} variations for each site, since atmospheric transport patterns may be random but surface fluxes are phase-locked

to the diurnal cycle. We note there are changes in surface fluxes in response to physical climate changes, such as thunderstorms/rain, cloud coverage, or boundary layer temperature, induced by mesoscale and synoptic-scale systems (Baldocchi et al., 2001). There is, however, no easy way to attribute the changes in X_{CO_2} and X_{H_2O} to either changing fluxes or synoptic/mesoscale transport without running a coupled atmosphere/land model. We choose instead to use an empirical, data-driven approach that necessitates neglecting weather-driven changes in surface fluxes.

For each calendar month, we binned all available observations (after removing the long-term trend) from the multi-year time series into half-hour increments to reveal the characteristic diurnal cycle (Fig. S1-2). For any given month, we limited our analysis to daytime observations obtained at solar zenith angle less than 75° to reduce the influence of spectroscopic errors at high air masses. We then removed the climatological daily cycle from each calendar day with observations, and assumed that the residual was the component of variability driven by transport. We note that this approach is a simplification, and expect that at least some of the residual were due to synoptic, intraseasonal, and interannual variability of surface fluxes. Our approach does, however, allow us to approximate the influence of local fluxes on the observations without relying on an ecosystem model or sparse flux tower data with limited spatial footprints

Given our assumption that temporal variability of X_{CO_2} and X_{H_2O} is derived from either local fluxes or atmospheric transport, we can then estimate the influence of atmospheric transport-driven variations from the time series of residuals. We calculated the standard deviation from the half-hourly bin averaged residuals at bi-weekly time intervals to approximate variability at synoptic and smaller timescales. We likewise calculated the standard deviation of the residuals within each day to approximate mesoscale variability. These time periods were sufficient to sample variability attributed to multiple synoptic scale weather systems, such as high and low pressure systems and frontal passages, or mesoscale systems, such as individual thunderstorms.

We evaluate our approach for calculating the influence of climatological fluxes on the diurnal cycle of X_{CO_2} at the Park Falls TCCON site since it is co-located with an Ameriflux eddy covariance (EC) tower that provides observations of diurnally varying NEE (Desai et al 2015). We estimate the influence that the observed eddy covariance fluxes have on the daily

cycle of X_{CO_2} (and denote this quantity as $X_{CO_2,EC}$ using equations 6 and 7:

$$\langle\frac{dX_{CO_2,EC}}{dt}\rangle = \frac{NEE_{EC} \cdot g \cdot MW_{dry\ air}}{P_s} \qquad \text{(Equation 6)}$$

$$X_{CO_2,EC} = \int_{\tau_{AM}}^{\tau_{PM}} \langle\frac{dX_{CO_2,EC}}{dt}\rangle d\tau \qquad \text{(Equation 7)}$$

where NEE_{EC} represents the observed net ecosystem exchange, g represents the gravitational constant of 9.81 ms^{-2}, $MW_{dry\ air}$ represents the molecular weight of dry air, P_s represents the surface pressure, and τ represents time. We calculated $X_{CO_2,EC}$ at hourly time steps over a period τ from when the local solar zenith angle crosses 70 degrees in the morning and afternoon. The seasonal cycle of the within-day variation in X_{CO_2} observed by the TCCON instrument agrees well with the seasonal cycle of the expected within-day variation in X_{CO_2} from NEE observations (R^2 of 0.8; Fig. 2a). The magnitude of the error bars derived from NEE, which represent the standard deviation among individual days, are substantially smaller than the magnitude of the error bars derived from the TCCON X_{CO_2} drawdown (Fig. 2b). During winter, the average standard deviation for $X_{CO_2,EC}$ is less than 0.1 ppm while the average standard deviation from $X_{CO_2,FTS}$ is about 0.4 ppm. In contrast, the average summer standard deviation is about 0.3 ppm for $X_{CO_2,EC}$ and 1.2 ppm for $X_{CO_2,FTS}$. Across seasons, the uncertainty from assuming a climatological within-day drawdown therefore reflects at most 30% of the total variability across the days on which observations are obtained. This suggests that most of the within-in day variation for X_{CO_2} results from processes other than local fluxes, confirming the motivation of the present study.
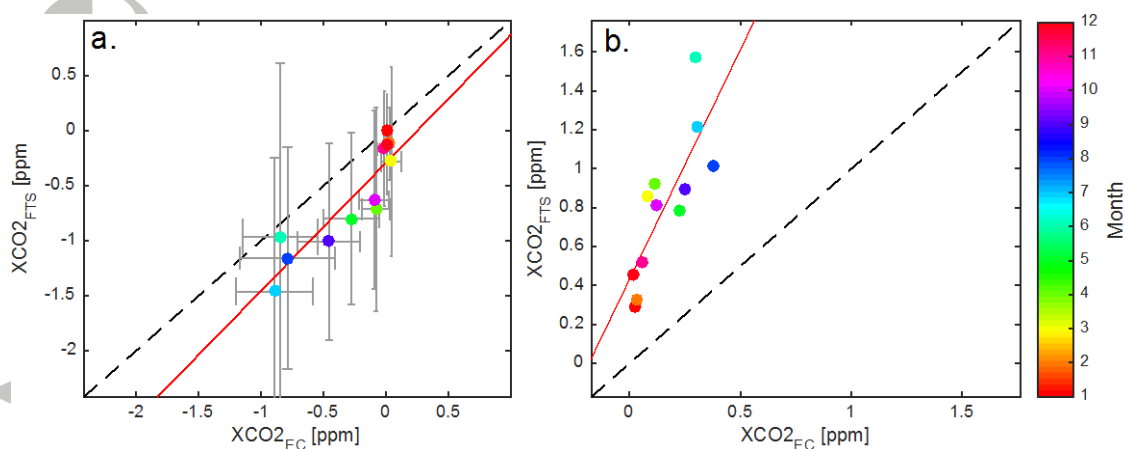

Figure 2. (*a.*) A comparison of the climatological monthly mean diurnal mean amplitude of

X_{CO_2} observed at the TCCON site ($X_{CO_2,FTS}$) compared to the estimated imprint of drawdown based on the observed net ecosystem exchange at the adjacent FluxNet eddy covariance tower in Park Falls, Wisconsin ($X_{CO_2,EC}$). (***b.***) The standard deviation of monthly mean $X_{CO_2,FTSS}$ compared to the standard deviation of $X_{CO_2,EC}$ plotted in panel **a**. Note that the axes in panel **b.** are different.

2.2 OCO-2

We analyzed spatial variations in X_{CO_2} and X_{H_2O} retrieved from OCO-2 satellite observations. OCO-2 is a sun-synchronous, polar-orbiting satellite with a spatial footprint for individual soundings of 2.4 km along-track and 1.25 km cross-track; the instrument measures 8 cross-track bins at each time step resulting in a narrow (~10 km wide) sampling swath (Eldering et al., 2017). The satellite acquires a repeat cycle of approximately every 16 days using three scanning modes, described below. The instrument comprises three grating spectrometers that measure radiances from reflected near-infrared sunlight in two CO₂ bands, the 1.61 weak absorption band (WCO₂) and the 2.06 μm strong CO₂ (SCO₂) absorption band, and in the 0.72 μm oxygen (O₂A) absorption band. These radiances are used in a full physics retrieval algorithm (version 8r, O'Dell et al., 2012; 2018), which uses optimal estimation to infer the vertical column of both CO₂ and O₂ while simultaneously adjusting other elements of the retrieval state vector, including the surface albedo for each band, aerosol optical depth (AOD), and other parameters that affect measured radiances (O'Dell et al., 2012; 2018). The reported error for each X_{CO_2} sounding is estimated using instrument noise, and then post-processed to account for errors associated with the forward model used in the retrieval algorithm (O'Dell et al., 2012; Wunch et al., 2017). The measurements are bias-corrected by accounting for biases in individual cross-track observations using multivariate linear regression to identify physically unrealistic correlations between X_{CO_2} and other elements of the retrieval state vector (such as surface pressure, aerosols, or unphysical variations of the retrieved vertical profile of CO₂) and systematic offsets of OCO-2 X_{CO_2} target mode retrievals in comparison to TCCON observations (O'Dell et al., 2018). The (lower bound) bias-corrected single sounding errors for retrieved X_{CO_2} are generally less than 1 ppm (compared to a mean global value of approximately 410 ppm; Tans and Keeling, 2018), with the largest errors over land and higher latitudes (generally above 45° N or S) and smallest errors over the ocean (Eldering et al., 2017). Similarly, X_{H_2O} was retrieved from OCO-2 using the 1.61 and 2.06 μm weak and strongly absorbing H₂O spectral bands with mean

biases of approximately 70 ppm, compared to typical X_{H_2O} concentrations that varies from roughly 700 to 9000 ppm globally (Nelson et al., 2016).

OCO-2 uses three scanning modes to optimize retrievals over land and ocean surfaces, including nadir (land only), glint (over ocean and land), where the instrument is pointed at the glint angle to maximize reflected light over water surfaces, and target where the instrument angle is adjusted to point towards a targeted location (typically a ground-based validation site). In this analysis, we investigate nadir and glint observations separately, and only used soundings without a quality warning flag (Osterman et al., 2018). In the figures, we report averages of nadir and glint observations since the only systematic differences were at coastal locations where there were not sufficient nadir observations. Note that many tracks exhibit significant missing data because of cloud cover.

2.2.1 Geostatistical analysis

We used geostatistical analysis to quantify the variance budget for OCO-2 data. We removed low frequency variations using a 250 km Hamming high-pass filter. To apply the filter, the data were pre-processed by averaging up to 8 cross-track soundings into 1.1 km bins in nadir mode or 1.3 km bins in glint mode to create a 1-dimensional track. We gap-filled empty bins with a distance-weighted mean of the nearest filled bin. For each 10° by 10° box, we filtered tracks containing valid observations in at least 96 bins in glint mode or 113 bins in nadir mode (i.e. one-half of the rolling window filter size). To minimize edge effects on the high-pass filter, we attached a 250-point buffer made up of the average of the first 250 bins (i.e. the length of variability passed through the high pass filter) to the beginning and end of each satellite track. After running the filter, we repopulated each sounding with the filtered bin-averaged and gap-filled values and began our semivariogram analysis described below.

We separated variance of X_{CO_2} and X_{H_2O} along OCO-2 tracks into random errors ("unexplained variance") and the component that is spatially coherent, or systematic, ("explained variance") by calculating semivariograms for the high frequency component of X_{H_2O} and X_{CO_2}. We calculated the semivariance (γ^*) for lag d at position x_k for sounding values Z using Equation 6,

$$\gamma^*(d) = \frac{1}{2N(d)} \sum_{k=1}^{N} [Z(\vec{x}_k) - Z(\vec{x}_k + d)]^2 \text{ (Equation 8)}$$

where N is the number of soundings separated by lag d (Cressie and Hawkins, 1980). We fit a spherical model (Equation 7) to estimate the total variance, c_∞, and the spatial range of total variance, denoted as a_{space} (as in equation 5), for each semivariogram (Fig. S3). For the spherical model fits, we fixed the unexplained variance, c_0, to the semivariance calculated from the observations at the smallest observed lag (1.1 km in nadir or 1.3 km in glint mode).

$$\gamma(d) = \begin{cases} c_0 + (c_\infty - c_0)\left[\frac{3d}{2a_{space}} - \frac{1d^3}{2a_{space}^3}\right] & \text{for } d \leq a_{space} \\ c_\infty & \text{for } d > a_{space} \end{cases} \quad \text{(Equation 9)}$$

We calculated the explained variance, denoted as $\langle c' \rangle_{space}$, by subtracting the unexplained variance from the total variance, $c_\infty\text{-}c_0$. In this framework, the explained variance relates to spatially coherent patterns, which could be due to real atmospheric gradients owing to fine scale transport or errors arising from spatially coherent correlations between X_{H_2O} and X_{CO_2} and other elements of the state vector. We compared the square root of unexplained and explained variances, denoted as unexplained and explained variability, to temporal variations observed at adjacent TCCON sites, described in more detail in Section 2.2.

2.2.2 North-south gradient calculation

To investigate the mesoscale tracer transport term on the RHS of Equation 5, we quantified the relationship between fine-scale spatial variations and the large-scale gradient in X_{H_2O} and X_{CO_2}. We calculated the North-South (N-S) gradient from three different datasets. For OCO-2, we aggregated data within a 10° by 10° box centered at the TCCON sites listed in Table 1. We calculated the gradient for each track within the targeted domain by fitting OCO-2 soundings to a simple least squares linear regression model weighted by self-reported errors from the version 8 level 2 retrieval algorithm. Because OCO-2 tracks may have data gaps associated with seasonal variations or cloud cover, we filtered the north-south gradients by quantifying the uncertainty (σ_{NS}^2) of the estimated N-S gradient using Equation 8 (Glover et al., 2011), where x_i represents the latitude and σ_i is the OCO-2 reported retrieval error at point i for N total soundings. We then discarded regression fits that had an uncertainty larger than 0.01 ppm degree^{-1}.

$$\sigma_{NS}^2 = \frac{\sum_{i=1}^N \frac{1}{\sigma_i^2}}{\sum_{i=1}^N \frac{1}{\sigma_i^2} \cdot \sum_{i=1}^N \frac{x_i^2}{\sigma_i^2} - \left(\sum_{i=1}^N \frac{x_i}{\sigma_i^2}\right)^2} \quad \text{(Equation 10)}$$

We compared monthly mean observed N-S gradients from OCO-2 to two additional datasets: the monthly mean N-S gradients derived from assimilated 2017 CarbonTracker (CT2017) output from the OCO-2 period (from 2014-2017, with observations ongoing) and the N-S gradients inferred from the High-Performance Instrumented Airborne Platform for Environmental Research (HIAPER) Pole-to-Pole Observations (HIPPO) flight transects over the Pacific Ocean that took place between 2009 and 2011. CarbonTracker is a data assimilation system that provides three-dimensional atmospheric CO_2 fields based on assimilating surface CO_2 observations from NOAA's cooperative sampling network (Peters et al., 2007; with updates documented at http://carbontracker.noaa.gov). X_{CO_2} was computed in their 2017 (CT2017) dataset with simple pressure-weighted vertical integration of CO_2. During the HIPPO campaign, partial columns of CO_2 were measured from roughly 300 to 8500 m altitude from aircraft transects spanning from 67°S to 85°N across the Pacific Ocean during all seasons between 2009 and 2011 (Wofsy et al., 2011). X_{CO_2} was then inferred by integrating a pressure-weighted mean concentration using reference static pressure from the GV Paroscientific Model 1000 sensor (Wofsy et al., 2017). We did not apply averaging kernels to either the CT2017 or HIPPO data since we were not attempting to directly compare individual columns to their OCO-2 or TCCON counterparts, but rather to approximate the large-scale features in X_{CO_2}.

With sufficient data density, the N-S gradients derived from OCO-2 overpasses were broadly consistent with CT2017 output and HIPPO transects. However, when satellite data were characterized by gaps or low coverage during the winter season, the satellite estimate of the N-S gradient was inconsistent with HIPPO and CarbonTracker. Given this pattern of agreement and the need for year-round N-S gradient information, we used the CarbonTracker gradient to quantify monthly-mean N-S gradients and to evaluate the impact of the gradient on temporal synoptic-scale and mesoscale variability and along-track high frequency explained variability.

3. Results

3.1 Temporal Variations at TCCON

3.1.1 Flux-driven diurnal variations

Local diurnal fluxes account for up to 1 to 2.0 ppm of within-day temporal variability of X_{CO_2}

during the growing season, with the largest diurnal signal observed during boreal summer (Fig. 3a). For example, in Lamont, Oklahoma, local ecosystem drawdown contributed a decrease of X_{CO_2} of 1.1 ppm between 7:00 am to 5:30 pm LST (local standard time) in July, whereas it showed almost no change throughout the day (10 am to 2 pm) during winter months (Fig. S1), as expected given the relatively dormant winter biosphere. At most midlatitude TCCON sites, local diurnal fluxes of X_{CO_2} accounted for less than 0.3 ppm of within-day variability during the winter (Fig. 3a). The seasonal cycle of X_{CO_2} variability driven by diurnal fluxes at tropical TCCON sites, such as Darwin, Australia, was tied to the onset of the wet and dry seasons and varied from 0.1 ppm and 1.1 ppm (Fig. 3a). We note that these are typical within-day variations of X_{CO_2} attributed to diurnal fluxes, and that the actual diurnal fluxes depend on weather, anthropogenic, and other natural interactions.
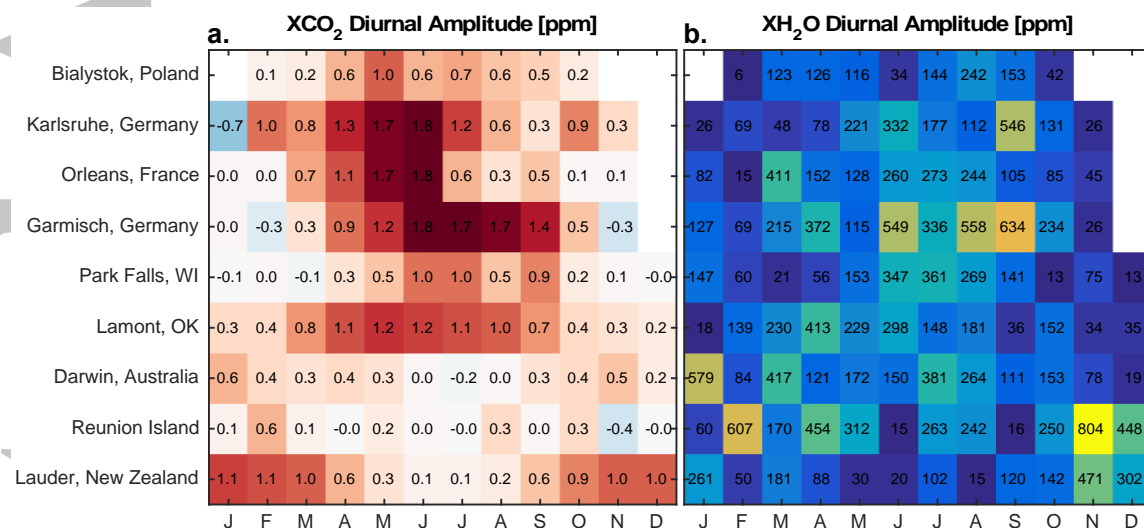
Figure 3. Climatological daytime diurnal range of **a.** X_{CO_2} and **b.** X_{H_2O} . We calculate the range between morning and evening, with a limit of solar zenith angle less than 75°.

The climatological diurnal cycle of X_{H_2O} had a strong seasonal cycle across all TCCON sites, with defined wet and dry seasons in the tropics, and lower winter and higher summer peak-to-trough diurnal cycle amplitudes in the midlatitudes (Fig. 3b). In the Northern Hemisphere midlatitudes, the within-day local imprint was maximum in the summer (around 200-600 ppm) and smallest during boreal winter (around 5-100 ppm). Within-day, flux-driven variations were largest at the two tropical TCCON sites, which are both located in the Southern Hemisphere tropics. Within-day variations in these regions could exceed 500 ppm during austral summer but were generally 300-500 ppm during austral winter (Fig. 3b). We

note that while many atmospheric processes are analogous for X_{CO_2} and X_{H_2O}, condensation and precipitation drive additional spatial and temporal variability in X_{H_2O} (Dai and Wang, 2002). The values we report in Fig. 3b are the peak-to-trough difference in within-day X_{H_2O} climatology. During summer, most TCCON sites showed a maximum value of X_{H_2O} in mid-to-late afternoon (1400 to 1700h, Fig. S2), consistent with the diurnal phasing of precipitable water reported by Dai and Wang (2002).
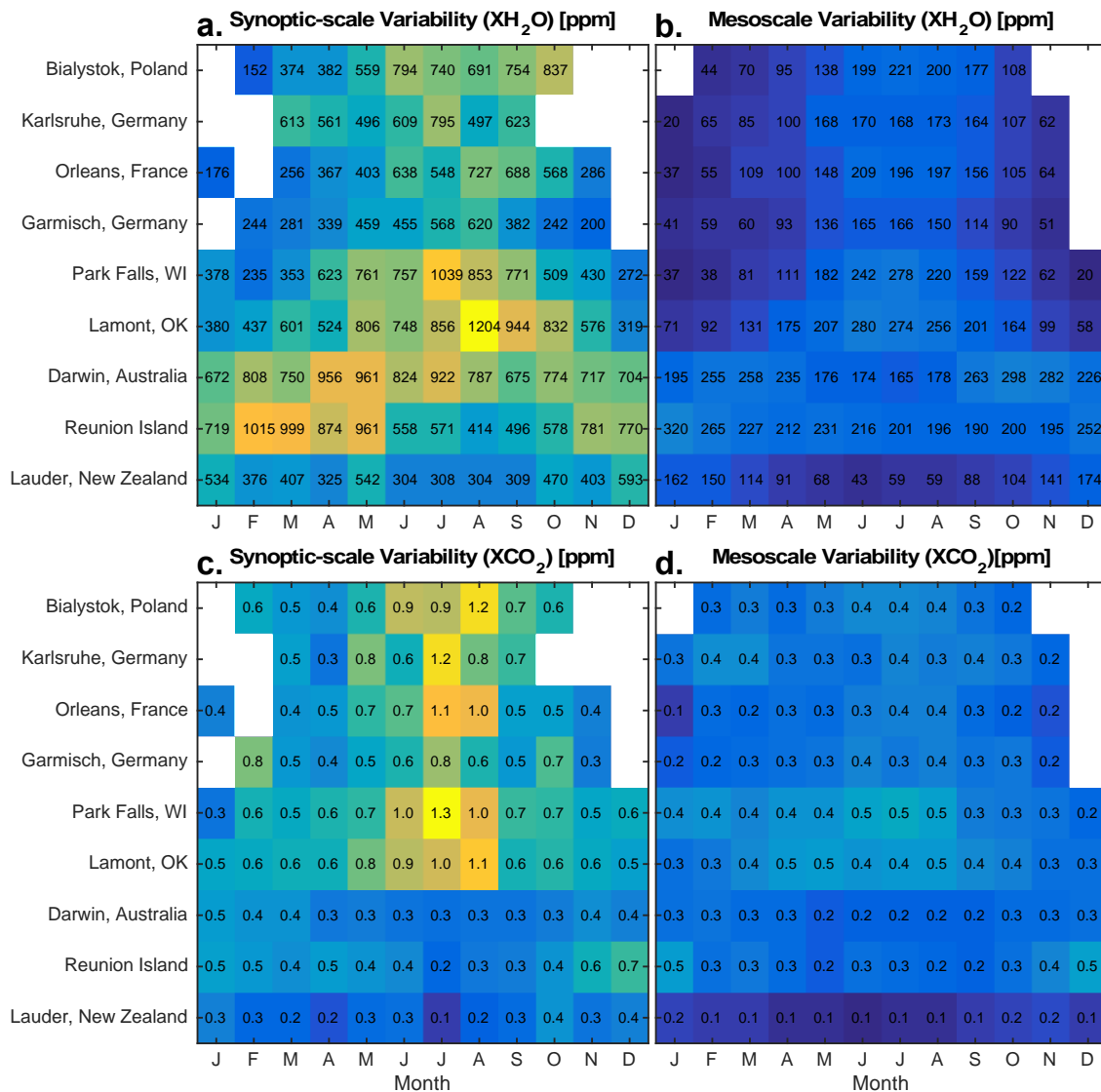
a. Synoptic-scale Variability (X_{H_2O}) [ppm]

Site	J	F	M	A	M	J	J	A	S	O	N	D
Bialystok, Poland		152	374	382	559	794	740	691	754	837		
Karlsruhe, Germany			613	561	496	609	795	497	623			
Orleans, France	176		256	367	403	638	548	727	688	568	286	
Garmisch, Germany		244	281	339	459	455	568	620	382	242	200	
Park Falls, WI	378	235	353	623	761	757	1039	853	771	509	430	272
Lamont, OK	380	437	601	524	806	748	856	1204	944	832	576	319
Darwin, Australia	672	808	750	956	961	824	922	787	675	774	717	704
Reunion Island	719	1015	999	874	961	558	571	414	496	578	781	770
Lauder, New Zealand	534	376	407	325	542	304	308	304	309	470	403	593

b. Mesoscale Variability (X_{H_2O}) [ppm]

Site	J	F	M	A	M	J	J	A	S	O	N	D
Bialystok, Poland		44	70	95	138	199	221	200	177	108		
Karlsruhe, Germany	20	65	85	100	168	170	168	173	164	107	62	
Orleans, France	37	55	109	100	148	209	196	197	156	105	64	
Garmisch, Germany	41	59	60	93	136	165	166	150	114	90	51	
Park Falls, WI	37	38	81	111	182	242	278	220	159	122	62	20
Lamont, OK	71	92	131	175	207	280	274	256	201	164	99	58
Darwin, Australia	195	255	258	235	176	174	165	178	263	298	282	226
Reunion Island	320	265	227	212	231	216	201	196	190	200	195	252
Lauder, New Zealand	162	150	114	91	68	43	59	59	88	104	141	174

c. Synoptic-scale Variability (X_{CO_2}) [ppm]

Site	J	F	M	A	M	J	J	A	S	O	N	D
Bialystok, Poland		0.6	0.5	0.4	0.6	0.9	0.9	1.2	0.7	0.6		
Karlsruhe, Germany			0.5	0.3	0.8	0.6	1.2	0.8	0.7			
Orleans, France	0.4		0.4	0.5	0.7	0.7	1.1	1.0	0.5	0.5	0.4	
Garmisch, Germany		0.8	0.5	0.4	0.5	0.6	0.8	0.6	0.5	0.7	0.3	
Park Falls, WI	0.3	0.6	0.5	0.6	0.7	1.0	1.3	1.0	0.7	0.7	0.5	0.6
Lamont, OK	0.5	0.6	0.6	0.6	0.8	0.9	1.0	1.1	0.6	0.6	0.6	0.5
Darwin, Australia	0.5	0.4	0.4	0.3	0.3	0.3	0.3	0.3	0.3	0.3	0.4	
Reunion Island	0.5	0.5	0.4	0.5	0.4	0.4	0.2	0.5	0.4	0.6	0.7	
Lauder, New Zealand	0.3	0.3	0.2	0.2	0.3	0.3	0.1	0.2	0.3	0.4	0.3	0.4

d. Mesoscale Variability (X_{CO_2}) [ppm]

Site	J	F	M	A	M	J	J	A	S	O	N	D
Bialystok, Poland		0.3	0.3	0.3	0.3	0.4	0.4	0.4	0.3	0.2		
Karlsruhe, Germany	0.3	0.4	0.4	0.3	0.3	0.3	0.4	0.3	0.4	0.3	0.2	
Orleans, France	0.1	0.3	0.2	0.3	0.3	0.3	0.4	0.4	0.3	0.2	0.2	
Garmisch, Germany	0.2	0.2	0.3	0.3	0.3	0.4	0.3	0.4	0.3	0.3	0.2	
Park Falls, WI	0.4	0.4	0.4	0.4	0.4	0.5	0.5	0.5	0.3	0.3	0.3	0.2
Lamont, OK	0.3	0.4	0.4	0.5	0.5	0.4	0.4	0.5	0.4	0.4	0.3	0.3
Darwin, Australia	0.3	0.3	0.4	0.3	0.2	0.2	0.2	0.2	0.2	0.3	0.4	
Reunion Island	0.5	0.3	0.3	0.3	0.2	0.3	0.3	0.2	0.2	0.3	0.4	0.5
Lauder, New Zealand	0.2	0.1	0.1	0.1	0.1	0.1	0.1	0.1	0.1	0.2	0.2	0.1

Figure 4. Comparison of synoptic-scale and variability in TCCON observations. (**a.**) X_{H_2O} monthly mean synoptic-scale (bi-weekly) variability, (**b.**) X_{H_2O} mesoscale (within-day) variability, (**c.**) X_{CO_2} monthly mean synoptic-scale variability, and (**d.**) X_{CO_2} monthly mean mesoscale variability. Note that the color scales for X_{H_2O} and X_{CO_2} are different.
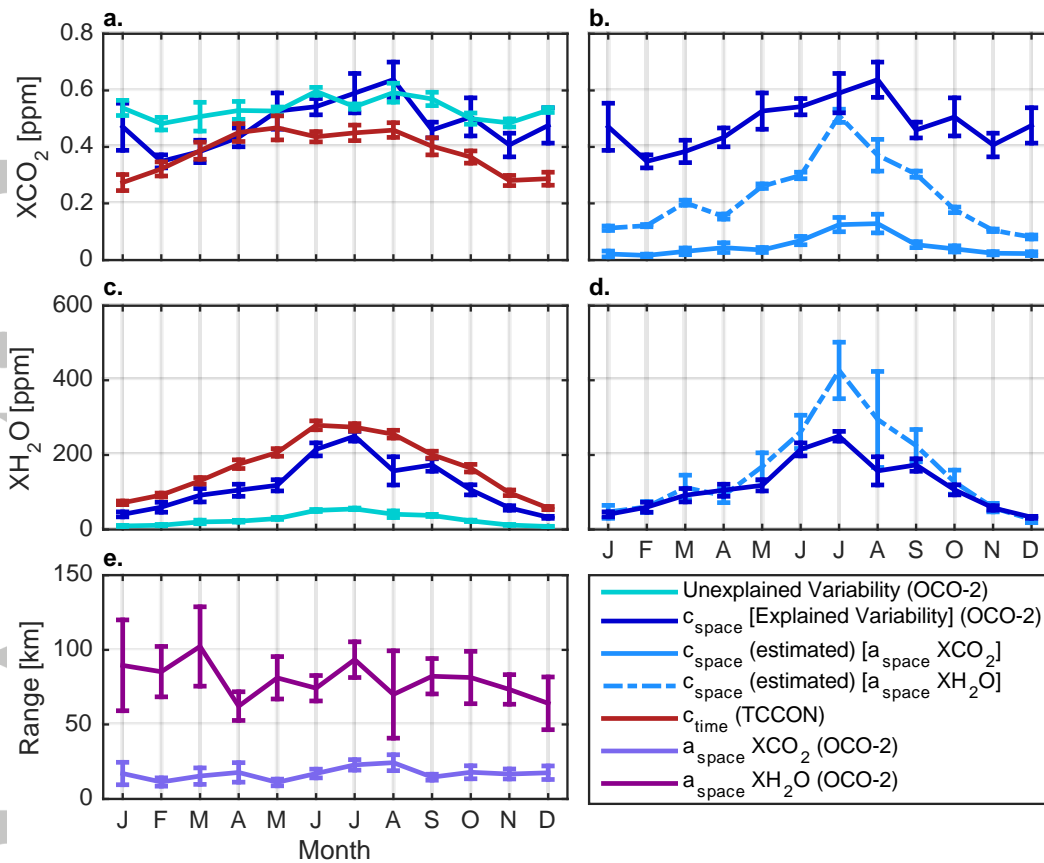
Figure 5. A comparison of monthly mean TCCON temporal mesoscale $\langle c' \rangle_{time}$ (within-day) variability *(red)*, OCO-2 observed along-track high frequency unexplained *(teal)* and explained ($\langle c' \rangle_{space}$) *(dark blue)* spatial variability, and explained variability ($\langle c' \rangle_{space}$) estimated from Equation 12 *(light blue)* using ranges (a_{space}) observed by OCO-2 for X_{H_2O} *(dashed line)* and X_{CO_2} *(solid line)*. Panels (**a.-b.**) shows variability for X_{CO_2} and panels (**c.-d.**) X_{H_2O} in Lamont, Oklahoma. The bottom panel, **e.**, represents the range (a_{space}) of along-track high frequency explained spatial variability of X_{H_2O} *(dark purple)* and X_{CO_2} *(light purple)*. The error bars for observed parameters represent the standard error. For estimated $\langle c' \rangle_{space}$, the error bars represent the error propagation using climatological monthly mean standard error of each observed parameter.

3.1.2 Synoptic-scale (bi-weekly) variability

Mean temporal synoptic-scale (bi-weekly) variations in both X_{H_2O} and X_{CO_2} from TCCON were larger in magnitude to the typical daily cycle (Fig. 3 and 4). For X_{H_2O}, synoptic-scale

variations were, on average, 4 times larger than variability attributed to diurnal fluxes (Fig. 3 and 4). For some months, synoptic-scale variability of X_{H_2O} was over 10 times larger than the magnitude of the imprint of local diurnal fluxes. For X_{CO_2} mean synoptic-scale variations were approximately twice as large local flux-driven variability, although for both gases, the differences varied seasonally. These variations in both X_{H_2O} and X_{CO_2} were also tied to the seasonal cycle in the large-scale N-S gradient (Table 2). As described in Section 2.2.1, we quantified temporal synoptic-scale variability by taking the standard deviation of the bi-weekly residual in X_{H_2O} and X_{CO_2} after accounting for the climatological peak-to-trough within-day signal at each TCCON site.

Temporal synoptic-scale variations of X_{H_2O} across all TCCON sites were of order 100 to 1000 ppm with strong regional and seasonal dependence (Fig. 4a). For example, we observe synoptic-scale variations in X_{H_2O} of 200-400 ppm in Lamont and Park Falls during boreal winter and peak synoptic-scale variability of over 1000 ppm during the Northern Hemisphere summer (Fig. 4a). At similar latitudinal regions in Europe, synoptic scale variability of X_{H_2O} only varies from 150 to 800 ppm throughout the year. We acknowledge that on multi-week timescales, many processes other than atmospheric transport can alter the atmospheric water vapor mole fraction, including diabatic processes in the atmosphere. This complexity is evident in the different seasonal patterns in and magnitudes of bi-weekly variability at TCCON sites, which varies even within a given latitude band. We therefore present this analysis to parallel the X_{CO_2} analysis described below.

For X_{CO_2}, typical synoptic-scale variations ranged from 0.1 to 1.3 ppm across all TCCON sites, with the largest variations (in excess of 1 ppm) observed over Northern Hemisphere TCCON sites during July and August (Fig. 4c). These locations also had the largest seasonal cycles of synoptic-scale variability (Fig. 4c). There was less pronounced synoptic-scale variability of X_{CO_2} in the tropics and the southern hemisphere, where synoptic-scale variability ranged from 0.1 in the boreal summer to 0.7 ppm in boreal winter (Fig. 4c). The magnitude and seasonality of these variations are mostly tied to the meridional (N-S) gradient in X_{CO_2}, as we discuss below.

Synoptic-scale variations of X_{CO_2} were correlated with the magnitude of the N-S gradient at northern hemisphere midlatitude TCCON sites (Table 2). As described in Section 2.3.2, we

fit a regression slope to estimate the absolute value of N-S gradients of X_{CO_2} derived from OCO-2 overpasses to those derived from CT2017 output and HIPPO transects (Fig. S4). In the Northern Hemisphere midlatitudes, the correlation between monthly mean temporal synoptic-scale variations observed from TCCON (Fig 4c.) and the monthly mean N-S gradient (Fig. S4-S6) was generally around 0.6 to 0.9 (Table 2). This relationship is consistent with the argument that synoptic variations arise from transient eddies acting on the large-scale gradient, as indicated by the second RHS term in Equation 5. The weaker correlation (R=0.41) observed at Garmisch, Germany was an outlier among Northern Hemisphere midlatitude TCCON sites, which may be due to limited observations. In the tropics and Southern Hemisphere, the relative absence of N-S gradients of X_{CO_2} resulted in weak relationship with synoptic-scale variations. We note that the length-scales estimated from many of the slopes of our best-fit linear regressions between synoptic scale variability and the N-S gradient of X_{CO_2} (2.1° to 6.5°; or roughly 200 to 600 km at Northern Hemisphere midlatitude TCCON sites) are on the smaller end of those of typical synoptic-scale systems.

The temporal synoptic variability of X_{H_2O} correlates with the N-S gradient of X_{H_2O} across most TCCON sites (Table 2). The correlation coefficients were between 0.4 to 0.9 across TCCON sites. The highest correlation coefficients were observed at mid-latitude TCCON sites (Bialystok, Orleans, Park Falls, and Lamont), and at these sites, the slope of the relationship was consistently between 7 and 9 ppm/(ppm/degree) (which can be written as a length scale, degree). This is approximately consistent with typical length scales of synoptic-scale variability of the order of magnitude of 1000 km and larger than that estimated for X_{CO_2}.

3.1.3 Mesoscale (within-day) variability

Mesoscale variations (Fig. 4b, 5c) of X_{H_2O} are, on average, a factor of 1.4 times larger in magnitude to variability attributed to local diurnal fluxes (Fig. 3b). For X_{H_2O}, mesoscale variations were generally a factor of 5 smaller than synoptic-scale variability across all TCCON sites (Fig. 4b). As expected based on synoptic scale variations in X_{H_2O}, patterns of mesoscale variation showed strong regional variations. For example, TCCON sites in North America (Park Falls and Lamont), mesoscale variations of X_{H_2O} were almost 300 ppm during the boreal summer, but less than 100 ppm during the boreal winter (Fig. 4b, 5c). In contrast, at TCCON sites at similar latitudes in Europe, mesoscale variations of X_{H_2O} were generally

less than 200 ppm all year. At tropical TCCON sites, such as Darwin and Reunion Island, mesoscale variations were between 160 and 320 ppm all year round, with lower (<200 ppm) mesoscale variations occurring during the dry season (Fig. 4b).

Mesoscale variations of X_{H_2O}, like synoptic variations, were generally correlated with the N-S gradient of X_{H_2O} across all midlatitude TCCON sites (R values of 0.4 to 0.9 at TCCON sites with statistically significant slopes; Table 2). The slopes, however, were much lower, typically around 2°. We expect that these correlations do not necessarily suggest that the large-scale N-S gradient drives mesoscale variations, but rather to the fact that both quantities change seasonally and have strong temperature dependence via the Clausius-Clapeyron relationship.

Temporal mesoscale variability in X_{CO_2}, which we assume is primarily driven by advection from small-scale weather features, was less than 0.5 ppm across all TCCON sites and all months (Fig. 4, 5). This represents about half the magnitude of variability attributed to local diurnal fluxes during the growing season at northern hemisphere TCCON sites (Fig. 4). In the winter, mesoscale variations of XCO2 become larger than the imprint of variability attributed to local diurnal fluxes. In Park Falls, Wisconsin, the combined imprint of mesoscale and synoptic scale transport was 1 to 2 ppm during summer (Fig. 4), substantially larger than the potential bias from assuming climatological fluxes of about 0.3 ppm (Fig. 2). These mesoscale variations were approximately 30 to 50% magnitude of synoptic-scale variability (Fig. 4c and 4d). Mesoscale variations in X_{CO_2} were only moderately correlated with N-S gradients (R-values less than 0.52) in the mid-to-high latitudes in both the northern and southern hemispheres (Table 2), consistent with our expectation that the length scale of mesoscale systems is small in comparison to the length scale of the N-S gradient. In the tropics, there was likewise no correlation between mesoscale variability and the N-S gradient of X_{CO_2} (Table 2).

We calculated a typical timescale for mesoscale (within-day) variations based on the autocorrelation of within-day residuals with climatological local fluxes removed (Fig. S7). We found that the autocorrelation of the residuals typically decayed to values between e^{-1} and 0 over about 3 hours. This timescale was consistent for both X_{H_2O} and X_{CO_2} across all TCCON sites. We therefore used this mean lag time as τ_{time} in Equation 5 to compare temporal variations to spatial variations of X_{H_2O} and X_{CO_2} (Section 3.2.1)

Table 2. Regression statistics for magnitude of variability in trace gases versus their N-S gradient. We report the slope (± 95% confidence interval) in units of degrees and the correlation coefficient, R, of a best-fit linear regression line for the N-S gradient of X_{H_2O} and X_{CO_2} output from CT2017 compared to bi-weekly (synoptic-scale) and within-day (mesoscale) temporal variability of X_{H_2O} observed by TCCON, and explained along-track high frequency spatial variability observed by OCO-2. Bolded slopes and regressions indicate statistically significant fits at the 95% confidence interval.

| Location	X_{H_2O}						X_{CO_2}					
	Synoptic (TCCON)		Mesoscale (TCCON)		Explained (OCO-2)		Synoptic (TCCON)		Mesoscale (TCCON)		Explained (OCO-2)	
	Slope [deg]	R	Slope [deg]	R	Slope [deg]	R	Slope [deg]	R	Slope [deg]	R	Slope [deg]	R
Bialystok, Poland	**7.4 ± 3.1**	**0.75**	**2.2 ± 0.5**	**0.92**	**1.3 ± 0.6**	**0.80**	**6.5 ± 5.2**	**0.44**	0.6 ± 1.6	0.06	-0.7 ± 4.0	0.01
Karlsruhe, Germany	1.5 ± 3.7	0.12	**1.8 ± 0.9**	**0.58**	**1.9 ± 1.3**	**0.64**	**2.9 ± 2.6**	**0.51**	0.4 ± 0.5	0.08	-0.0 ± 0.7	0.00
Orleans, France	**7.6 ± 3.4**	**0.69**	**1.9 ± 1.2**	**0.50**	0.7 ± 1.6	0.11	**3.1 ± 1.2**	**0.76**	0.7 ± 0.4	0.52	-0.4 ± 0.9	0.13
Garmisch, Germany	3.5 ± 3.7	0.28	**1.4 ± 1.0**	**0.42**	**2.1 ± 1.0**	**0.72**	0.8 ± 1.2	0.17	**0.4 ± 0.3**	**0.29**	-0.3 ± 1.4	0.02
Park Falls, WI	**7.5 ± 2.2**	**0.79**	**2.7 ± 0.6**	**0.87**	**1.5 ± 1.2**	**0.41**	**3.6 ± 1.6**	**0.62**	**0.9 ± 0.8**	**0.30**	0.3 ± 1.2	0.04
Lamont, OK	**8.7 ± 6.9**	**0.35**	1.5 ± 2.4	0.12	1.1 ± 2.2	0.08	**2.1 ± 0.9**	**0.67**	0.5 ± 0.5	0.32	**0.8 ± 0.4**	**0.49**
Darwin, Australia	**0.8 ± 0.5**	**0.46**	**0.3 ± 0.2**	**0.39**	**-0.4 ± 0.3**	**0.36**	**1.1 ± 0.7**	**0.41**	0.4 ± 0.4	0.27	0.3 ± 1.0	0.04
Reunion Island	4.6 ± 6.2	0.15	0.8 ± 1.2	0.12	1.1 ± 1.2	0.23	-1.0 ± 3.7	0.02	-0.7 ± 3.0	0.02	0.4 ± 1.1	0.04
Lauder, New Zealand	**4.5 ± 3.7**	**0.33**	**2.8 ± 1.1**	**0.69**	**0.7 ± 0.6**	**0.58**	4.1 ± 9.5	0.06	2.5 ± 3.6	0.14	0.2 ± 9.9	0.00
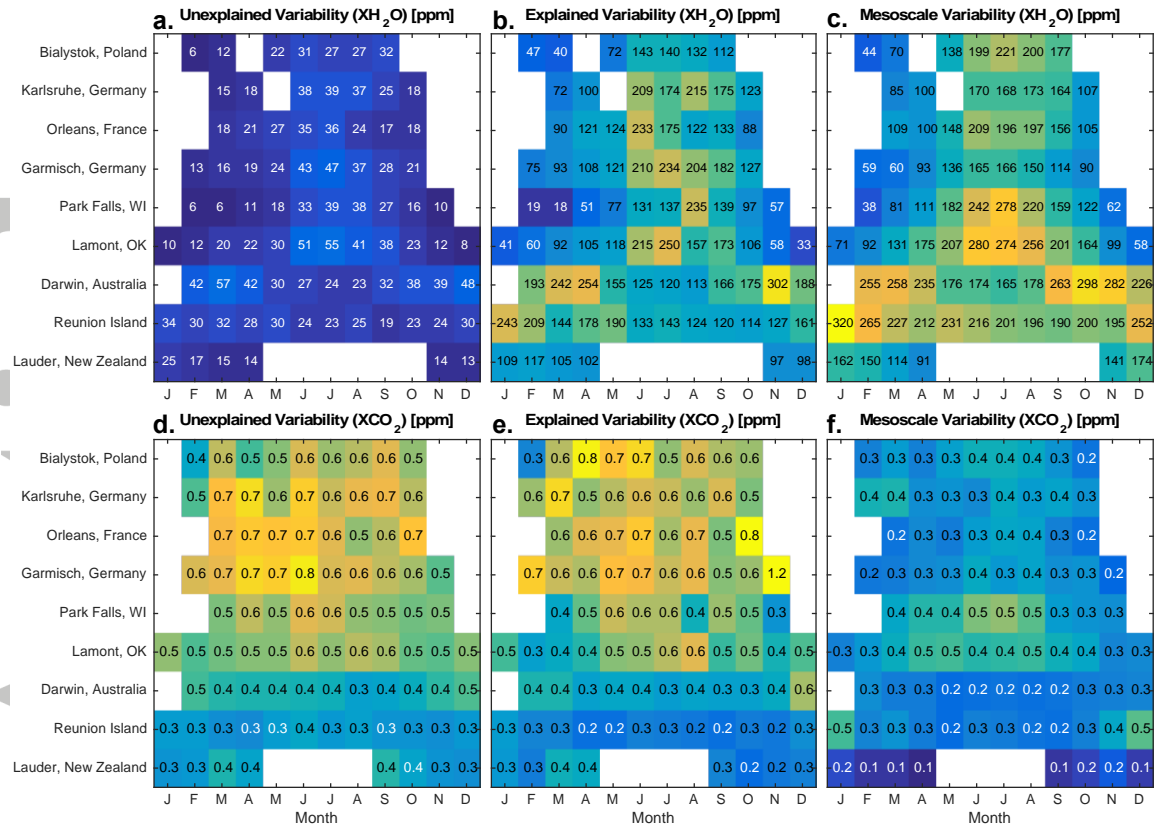
Figure 6. Variability metrics for remotely sensed X_{H_2O} and X_{CO_2}. Monthly mean (**a.**) unexplained variability for X_{H_2O} and (**b.**) explained variability for X_{H_2O} derived from high-pass filtered OCO-2 observations. **c.** Monthly mean temporal mesoscale (within-day) variability in X_{H_2O} derived from TCCON observations. Panels **d-f** are similar, except we show values for X_{CO_2} from OCO-2 (d-e) and TCCON (f) observations.
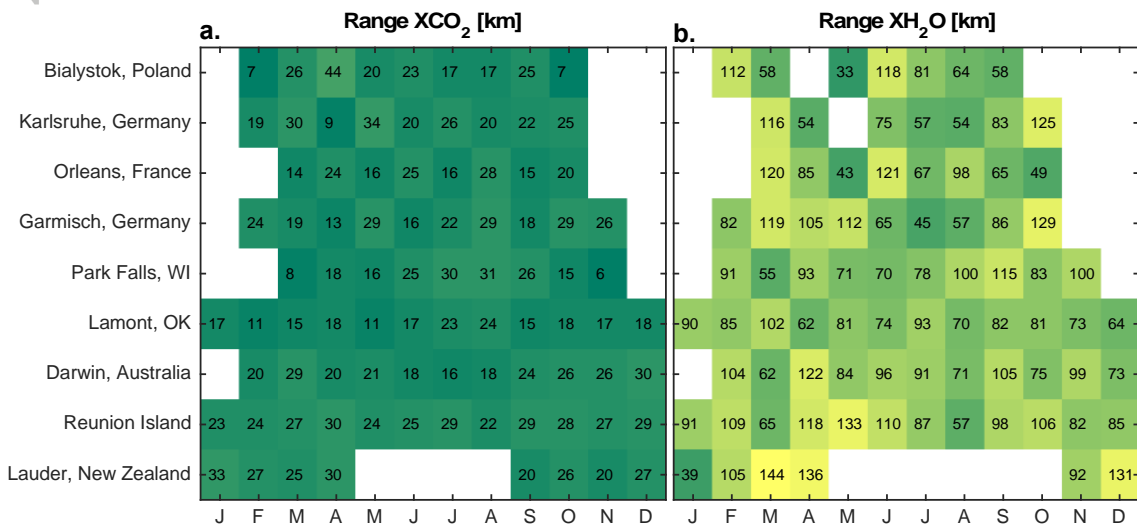

Figure 7. Monthly mean spatial range (a_{space}) of **a.** X_{H_2O} and **b.** X_{CO_2} derived from OCO-2 data near each TCCON site. Note both panels use the same color scale.

3.2 OCO-2 along-track spatial variability

This section compares the relationship between the high-frequency along-track spatial variability observed by OCO-2 to mesoscale temporal variability of X_{H_2O} and X_{CO_2} from TCCON using the theoretical framework outlined in Section 2.1. Variations in both X_{H_2O} and X_{CO_2} evolve in response to local surface fluxes and atmospheric transport, and for X_{H_2O}, condensation, evaporation, and precipitation within the atmosphere. While the details of the surface fluxes and in situ atmospheric processes differ for the two tracers, they experience the same atmospheric advection and mixing fields. The advantage of a joint analysis of these two gases is that both X_{H_2O} and X_{CO_2} are observed simultaneously by TCCON and OCO-2, and the precision of X_{H_2O} is substantially larger, providing a framework for assessing the X_{CO_2} results. Specifically, if the calculated and observed explained variability of either species, $\langle c' \rangle_{space}$, are in agreement, then we can assume that mesoscale atmospheric transport is the dominant source of high-frequency variability of that gas.

3.2.1 Explained variability ($\langle c' \rangle_{space}$)

Along-track, high frequency (<250 km) explained spatial variations of X_{H_2O} from OCO-2 spanned between 20 and 300 ppm across all TCCON sites (Fig. 6b). The smallest explained variations (20 to 60 ppm) were observed at Northern Hemisphere midlatitude sites during the boreal winter. The largest explained variations (> 200 ppm) occurred over most Northern Hemisphere midlatitude sites during the boreal summer and over the tropical sites (Darwin and Reunion Island) during the local wet season. Across all months and TCCON sites, the spatial range (a_{space}) of explained variability generally spanned between 40 to 140 km (Fig. 7b).

The explained high-frequency spatial variability of X_{CO_2} was generally between 0.2 and 1.0 ppm across all TCCON sites (Fig. 6e). The highest explained variations (>0.5 ppm) were observed over Northern Hemisphere TCCON sites. Smaller explained variations (0.2 to 0.5 ppm) were observed at southern hemisphere TCCON sites. In contrast to X_{H_2O}, the a_{space} for X_{CO_2} occurred at much smaller spatial scales from 10 to 40 km, with mean a_{space} values for explained variability around 20 km (Fig. 7a).

We can put the explained spatial variability of both X_{H_2O} and X_{CO_2} along OCO-2 tracks

($\langle c' \rangle_{space}$) by comparing variations in each gas with the corresponding mesoscale variations at TCCON sites (Section 2.3.1) using Equation 5 to relate temporal variations at a given location to tracer anomaly advection and turbulent production. We expect the time tendency (Term A in Equation 9) to be balanced by the advection of tracer variations by the mean wind (Term B) or by small-scale production of variation by eddies acting on the mean gradient (Term C). Take, for example, a typical temporal mesoscale variation of X_{H_2O}, $\langle c' \rangle_{time}$, of about 280 ppm (as is approximately the case in Lamont, Oklahoma in June; Figs. 4-6). We computed the following scales:

$$(\text{A}) \; \frac{\langle c' \rangle_{time}}{\tau_{time}} = \frac{280 \text{ ppm}}{3 \text{ hours}} = 90 \frac{\text{ppm}}{\text{hour}}$$

$$(\text{B}) \; \overline{u} \frac{\langle c' \rangle_{space}}{a_{space}} = 8 \left(\frac{\text{m}}{\text{s}} \right) \frac{210 \text{ ppm}}{70 \text{ km}} = 90 \frac{\text{ppm}}{\text{hour}}$$

$$(\text{C}) \; \langle u' \rangle \langle \frac{\partial \overline{c}}{\partial x} \rangle = 1 \left(\frac{\text{m}}{\text{s}} \right) \left(140 \frac{\text{ppm}}{\text{deg.}} \right) = 5 \frac{\text{ppm}}{\text{hour}}$$

We used a within-day period (τ_{time}) of 3 hours (Section 3.1.3; Fig. S7). For Lamont in June, we computed total column pressure and H_2O vertical profile weighted mean horizontal wind speed ($\overline{u}$) of 8 m/s and mesoscale variability of horizontal winds (u') of 1 m/s by vertically integrating wind output from CT2017 (Fig. S8). Since CarbonTracker is run at relatively coarse resolution, we compare these values against calculations derived from the North American Regional Reanalysis (NARR, Mesinger et al., 2006), which provides wind fields at 0.3 degrees resolution. At the two North American TCCON sites, u was the same as that estimated from CarbonTracker fields, while u' was larger by a factor of two (about 2 m/s), an expected result given the higher horizontal resolution of NARR. Nevertheless, when we apply this larger u' estimate into Equation 11, our scale analysis remains unchanged. We also used CT2017 output to calculate a typical summertime Northern Hemisphere midlatitude N-S gradient of around 140 ppm degree[-1] (Fig. S5). The scaling exercise suggests that the time tendency is mostly balanced by the mesoscale anomaly advection term (Term B) rather than the turbulent production term (Term C), at least for these time-scales. The small contribution of the production term is consistent with the fact that mesoscale variations at TCCON sites were not highly correlated with the mean N-S gradient. This analysis can also be applied to relate spatial and temporal mesoscale variations in X_{CO_2} or another atmospheric tracer.

Based on the scaling arguments above, we rearrange Equation 5 to solve for the expected $\langle c' \rangle_{space}$ along OCO-2 tracks and neglect the turbulent production term (Equation 12):

$$\langle c' \rangle_{space} = \frac{a_{space}}{\bar{u}} \left(\frac{\langle c' \rangle_{time}}{\tau_{time}} - \langle u' \rangle \langle \frac{\partial \bar{c}}{\partial x} \rangle \right) \approx \frac{a_{space}}{\bar{u}} \left(\frac{\langle c' \rangle_{time}}{\tau_{time}} \right). \text{(Equation 12)}$$

We then use Equation 12 to estimate the expected magnitude of $\langle c' \rangle_{space}$ for X_{H_2O} in Lamont in June as approximately 226 ppm which agrees within 10% with the observed explained variability of 214 ppm from OCO-2 (Fig. 6b and 8b). We found that if we applied Equation 12 to compute $\langle c' \rangle_{space}$ at each TCCON site and each month, our estimated $\langle c' \rangle_{space}$ values match observed explained variations from OCO-2 to within 30% (Fig. 8a and 8b). The agreement between the observed and estimated $\langle c' \rangle_{space}$ of X_{H_2O} suggests that the observed explained variations of X_{H_2O} from OCO-2 are primarily driven by mesoscale atmospheric transport (Fig. 5 and 8a,b). These results also validate our choice of a 250 km high-pass filter to isolate mesoscale transport and exclude larger-scale synoptic systems.

We likewise calculated the $\langle c' \rangle_{space}$ of X_{CO_2} in Lamont in June using the estimated total column pressure and CO_2 vertical profile weighted mean horizontal wind speed ($\bar{u}$) m/s and a spatial range, a_{space}, of 20 km fit from semivariogram analysis (Fig. 7a). Using this framework, the calculated spatial mesoscale variability of 0.1 ppm was much smaller than the observed $\langle c' \rangle_{space}$ (0.6 ppm). The empirical a_{space} of 20 km for X_{CO_2} is suspect, since mesoscale variations in X_{H_2O} from OCO-2 showed an a_{space} of 70 km in the same month and are consistent with the expected length-scale for mesoscale systems. When we instead used a_{space} of 70 km based on the analysis of X_{H_2O}, estimated mesoscale variability increases to 0.3 ppm (Equation 14).

$$\langle c' \rangle_{space, X_{CO_2}} = \frac{70 \text{ km}}{10 \frac{\text{m}}{\text{s}}} \left(\frac{0.4 \text{ ppm}}{3 \text{ hours}} \right) \cong 0.3 \text{ ppm (Equation 14)}$$

We note that an estimate of 0.3 ppm, while more reasonable in magnitude, is still about 40% smaller than the observed value of 0.5 ppm for the OCO-2 explained X_{CO_2} variability.
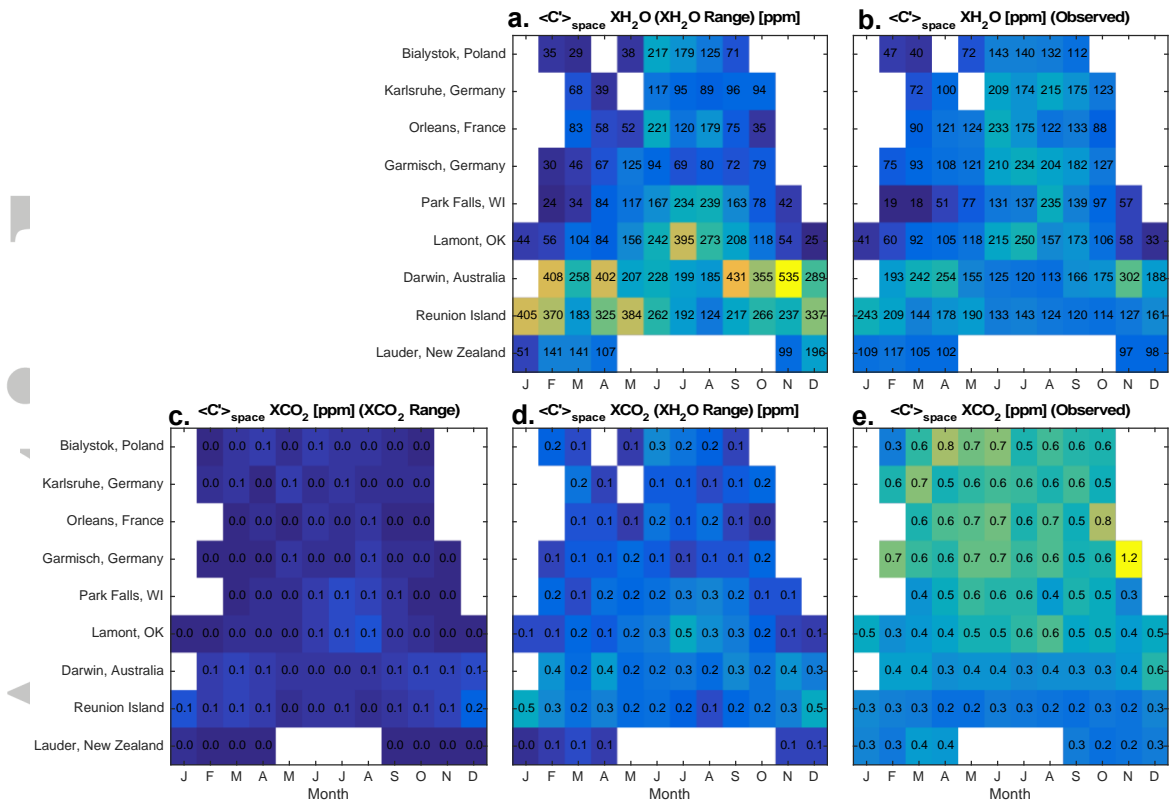
Figure 8. Comparison of calculated and observed $\langle c' \rangle_{space}$. The top row shows (**a.**) Calculated annual cycle in $\langle c' \rangle_{space}$ for X_{H_2O} using Equation 12, assuming a_{space} values derived from X_{H_2O} (Figure 7b) and $\langle c' \rangle_{time}$ values from TCCON mesoscale variations (Fig. 4b). (**b.**) Observed annual cycle in $\langle c' \rangle_{space}$ for X_{H_2O}. Note that this quantity is identical to the explained variability of X_{H_2O} (Figure 6b). The bottom row shows the same quantities, except for X_{CO_2}. (**c.**) Calculated annual cycle in $\langle c' \rangle_{space}$ for X_{CO_2} using Equation 12, assuming a_{space} values for X_{CO_2} (Fig. 7a) and $\langle c' \rangle_{time}$ values from TCCON (Fig. 4d). (**d.**) Calculated annual cycle in $\langle c' \rangle_{space}$, except we use a_{space} values from X_{H_2O}. (**e.**) Observed annual cycle in $\langle c' \rangle_{space}$ for X_{CO_2} (identical to Fig. 6e).

Together, these relationships suggest first that the temporal and spatial scaling within our framework is consistent with mesoscale variations of X_{H_2O} quantified using TCCON and OCO-2 data. Second, the spatial range (a_{space}) for X_{CO_2} variability derived from the geostatistical analysis of OCO-2 data is too small to be driven by mesoscale systems. Third, the results suggest that the X_{CO_2} $\langle c' \rangle_{space}$ value is larger than what is calculated assuming mesoscale systems are the only driver of high frequency spatial variability along OCO-2 tracks. As shown for Lamont, Oklahoma, there is no overlap between the estimated and

observed $\langle c' \rangle_{space}$ even when accounting for uncertainty in both terms (Fig. 5b). We estimated the uncertainty $\langle c' \rangle_{space}$ using error propagation of the standard error of each of the measured terms in equation 12. Although we only plot the uncertainty on the $\langle c' \rangle_{space}$ calculation for Lamont (Fig. 5), we quantified uncertainty across all TCCON sites presented in the paper and this result is robust, meaning that the differences between the calculated $\langle c' \rangle_{space}$ (Fig. 8c,d) and the observed $\langle c' \rangle_{space}$(Fig. 8e) represent real and significant disagreement. Thus, we conclude that some other factor imparts spatially coherent variability on OCO-2 X_{CO_2} that depresses the a_{space} and augments the $\langle c' \rangle_{space}$. One possibility is coherent biases or errors in the OCO-2 X_{CO_2} retrieval, as discussed more in section 3.3. These relationships are true across all TCCON sites (Fig. 8c and 8e), where the observed X_{CO_2} $\langle c' \rangle_{space}$ was generally larger than what would be expected based on $\langle c' \rangle_{time}$ and the observed X_{CO_2} a_{space} was small relative to the value calculated from X_{H_2O} observations (Fig. 8a and 8b). We found that X_{CO_2} $\langle c' \rangle_{space}$ was more comparable to observed explained variations from OCO-2 when we used observed a_{space} values for X_{H_2O} (Fig. 8d and 8e).

We do not expect that the inflated X_{CO_2} $\langle c' \rangle_{space}$ values result from aliasing of synoptic scale variability. First, the water vapor analysis confirmed that our 250 km filter properly isolates mesoscale atmospheric transport. Second, the explained variability from OCO-2 was not correlated with the N-S gradients (Table 2). If our $\langle c' \rangle_{space}$ values reflected synoptic scale variability, these quantities should be correlated.

3.2.2 Unexplained variability

The unexplained high frequency spatial variability of X_{H_2O} was up to 50 ppm (Fig. 5 and 6), about 50% larger than the random errors reported by the v8 OCO-2 retrieval algorithm data product. These results were consistent with arguments from Connor et al. (2008) that reported random errors from the OCO-2 retrieval algorithm represent a lower bound on actual error. However, our estimate for unexplained variability along OCO-2 tracks was still less than 20% of the temporal and spatial mesoscale X_{H_2O} variability (Fig. 5 and 6), suggesting that the signal-to-noise ratio of X_{H_2O} retrievals are large enough to observe mesoscale variations.

The unexplained spatial variability in X_{CO_2} was 0.3 to 0.8 ppm, which is the same order of magnitude as the spatial and temporal variations that may reflect mesoscale variations and is also generally consistent with random errors reported by the v8 OCO-2 retrieval algorithm

data product (Fig. 6d). These unexplained variations were consistent with the mean standard deviation of the cross-track soundings we averaged into each along-track bin (Section 2.3.2; Fig. S9). OCO-2 tracks adjacent to Southern Hemisphere TCCON sites typically had smaller unexplained variations (0.3-0.4 ppm), while tracks adjacent to Northern Hemisphere TCCON sites had slightly larger unexplained variations (0.5-0.7 ppm). This difference appears to arise due to the fact that the Southern Hemisphere and tropical OCO-2 tracks we analyzed contained ocean observations, whereas the Northern Hemisphere tracks contained only land observations. When we conducted semivariogram analysis around the latitude band between 40-50 degrees North, the unexplained variations over the ocean were approximately half the magnitude observed over land (Fig. 9). Errors associated with retrieving X_{CO_2} over land, where topography and albedo can influence the X_{CO_2} retrieval, likely increase the unexplained variability. The unexplained variations over land did not show dependence on nadir versus glint observing mode. We note that the estimates for unexplained variability were not sensitive to the cutoff for the high-pass filter and were also robust when we explicitly fitted, rather than fixed, the unexplained variance in the spherical semivariogram model.
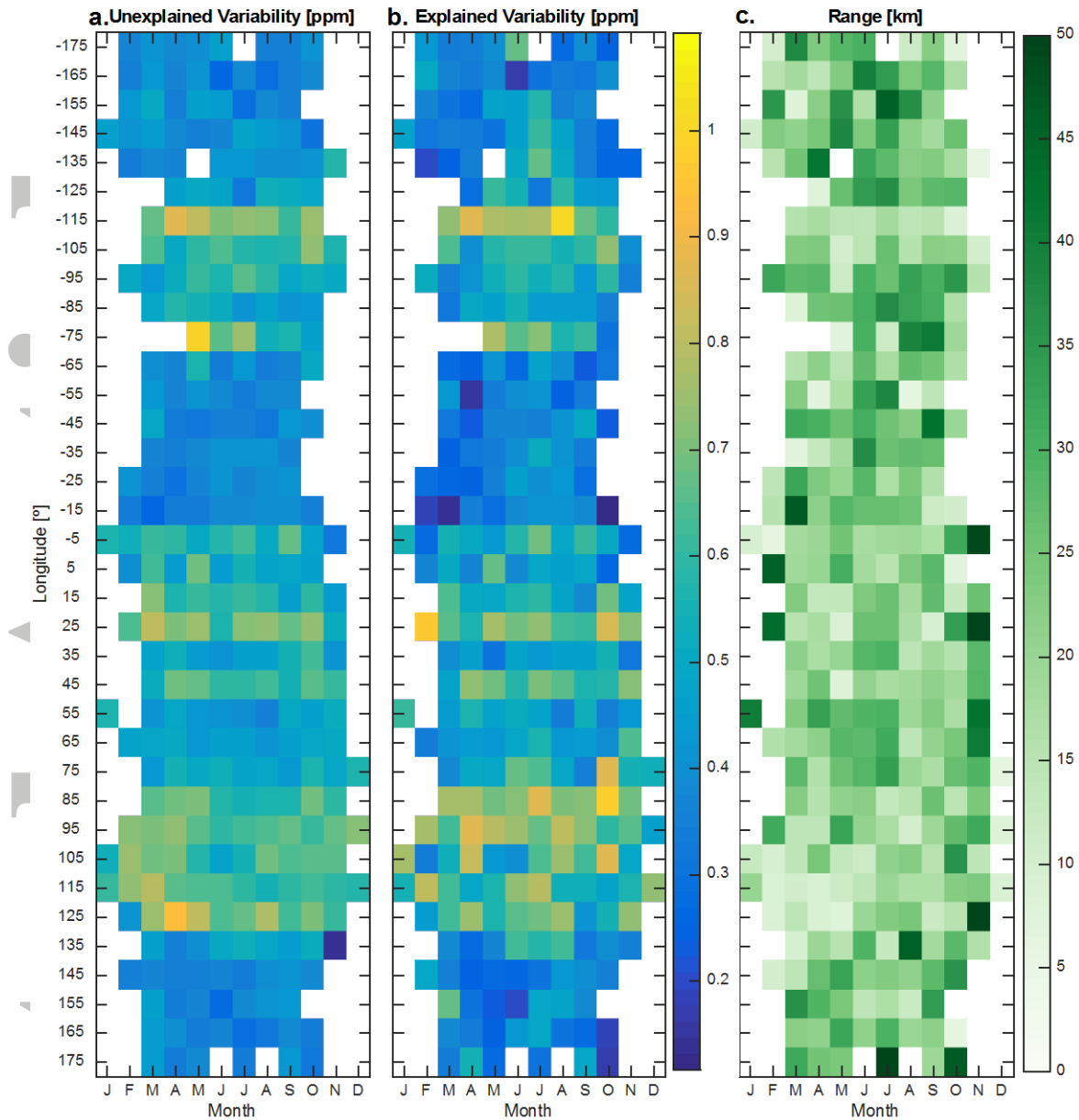
Figure 9. Global analysis of along-track high-frequency spatial (**a.**) unexplained variability, (**b.**) explained variability, and (**c.**) range of explained variability (a_{space}) of X_{CO_2} within 10° × 10° grid cells across a latitudinal band centered at 45°N. In general, grid cells over ocean show lower values of explained and unexplained error than those over land.

3.3 Spatially correlated variance from the state vector

Correlations between high frequency along-track spatial variations in X_{CO_2} and other elements of the OCO-2 retrieval state vector likely contributed to the larger than expected spatially coherent (explained) variability in OCO-2 X_{CO_2}, compared to mesoscale variations

at corresponding TCCON sites (Table 4), and the smaller geostatistical spatial range (a_{space}) for X_{CO_2} than X_{H_2O}. We therefore tested whether the total and high frequency along-track spatial variability of X_{CO_2} were correlated with other elements of the OCO-2 retrieval state vector. We selected aerosol optical depth (AOD) and albedo in the O_2 and weak and strong CO_2 absorption bands as variables that were likely to have spatial structures that, if correlated with X_{CO_2}, could obscure spatially coherent transport patterns. The correlations between elements of the state vector and both the total variations and the high frequency along-track spatial variations of X_{CO_2} were small (R ≤ 0.2; Table 3), but statistically significant. This analysis suggests that correlations between X_{CO_2} and these state vector elements may have depressed the apparent a_{space} and increased the explained variability along OCO-2 tracks. We note that the analysis of albedo and AOD presented here was in no way exhaustive, but rather, our results show that these correlations were important contributors to the overall variance budget.

In contrast, high frequency variations in X_{H_2O} were generally independent of other state vector elements. There were some weak to moderate, statistically significant correlations between the unfiltered X_{H_2O} data and albedo or AOD (Table 3). These correlations could represent real geophysical relationships among X_{H_2O}, albedo, and AOD, but could also be attributed large-scale, coherent systematic biases in the retrieval of X_{H_2O} that can be attributed to errors in AOD and albedo. When we high-pass filtered these variables, however, the correlations between the high frequency variations of X_{H_2O} and albedo were not statistically significant, with the exception of AOD. This result suggests that at smaller spatial scales (less than 250 km), the variations in X_{H_2O} were independent of the state vector elements we tested here and therefore the explained variability did not contain the imprint of spatially coherent biases

Table 3. Mean correlation coefficients between OCO-2 trace gases and other elements of the state vector, including aerosol optical depth (AOD), and surface albedo in the oxygen-absorbing band (O_2A), weakly absorbing CO_2 band (WCO_2), and strongly absorbing CO_2 band (SCO_2) retrieved from OCO-2 observations. Bolded values denote statistically significant non-zero mean correlation coefficients at a 95% confidence interval.

Location	X_{H_2O}								X_{CO_2}							
	Total Variability				High Frequency Variability				Total Variability				High Frequency Variability			
	AOD	O_2A	WCO_2	SCO_2	AOD	O_2A	WCO_2	SCO_2	AOD	O_2A	WCO_2	SCO_2	AOD	O_2A	WCO_2	SCO_2
Bialystok, Poland	**0.24**	0.11	**0.14**	**0.13**	**0.12**	0.02	0.05	0.05	**0.09**	**0.15**	**0.12**	0.06	**0.08**	**0.13**	**0.12**	**0.05**
Karlsruhe, Germany	**0.18**	0.07	0.09	0.08	**0.12**	-0.01	0.01	0.02	**0.16**	**0.12**	0.07	0.04	**0.11**	**0.12**	**0.08**	0.03
Orleans, France	**0.13**	0.09	**0.14**	**0.16**	**0.07**	0.01	0.06	**0.09**	**0.20**	**0.17**	**0.13**	**0.11**	**0.17**	**0.16**	**0.14**	**0.09**
Garmisch, Germany	**0.17**	-0.01	**0.10**	**0.10**	**0.11**	0.01	**0.07**	**0.08**	**0.13**	**0.09**	0.05	0.02	**0.10**	**0.09**	**0.06**	0.02
Park Falls, WI	**0.14**	0.09	**0.16**	**0.13**	**0.07**	0.04	**0.10**	**0.09**	**0.10**	**0.11**	**0.10**	0.07	**0.08**	**0.12**	**0.14**	**0.09**
Lamont, OK	0.06	0.00	**-0.14**	**-0.14**	**0.04**	0.03	-0.01	0.00	**0.14**	**0.07**	**0.06**	0.04	**0.06**	**0.13**	**0.16**	**0.12**
Darwin, Australia	0.03	**-0.32**	**-0.40**	**-0.41**	0.01	-0.01	0.00	-0.01	**0.07**	0.01	-0.02	-0.03	0.03	**0.06**	0.04	0.01
Reunion Island	**0.18**	-0.03	**-0.13**	**0.12**	**0.08**	0.03	0.00	**0.05**	**-0.07**	**0.07**	0.04	**0.14**	**-0.09**	**0.09**	0.07	**0.18**
Lauder, New Zealand	**0.14**	-0.05	**-0.13**	0.03	**0.08**	0.02	-0.03	0.02	**0.16**	0.02	0.06	**0.12**	0.02	-0.03	**-0.08**	-0.04

4. Discussion and Conclusions

We developed a framework that allows us to leverage spatially dense soundings from the OCO-2 satellite and temporally dense soundings from TCCON to quantify the variance budget for X_{H_2O} and X_{CO_2}, with a focus on estimating the imprint of mesoscale transport on OCO-2 observations. We first developed a method to separate variations from local diurnal surface-atmosphere fluxes, synoptic-scale atmospheric transport, and mesoscale atmospheric transport from the overall variability in TCCON observations. We found that variability from synoptic-scale transport was, on average, 3 times larger than that attributed to diurnal fluxes for X_{H_2O} and of 2 times larger magnitude for X_{CO_2}. On average, and mesoscale variations in X_{H_2O} and X_{CO_2} were similar in magnitude to the variability from local diurnal fluxes. The large contributions of mesoscale and synoptic scale transport in driving tracer variability underscores the importance of accounting for uncertainties in atmospheric transport and its subgrid-scale impact when using X_{CO_2} in a carbon flux inference system.

Second, we used geostatistical analysis to quantify explained (spatially coherent) and unexplained (random) variations in X_{CO_2} and X_{H_2O} along OCO-2 tracks. We applied a 250-km high pass filter that, for X_{H_2O}, isolated mesoscale variations that were the primary driver of along-track high frequency variability of X_{H_2O} from OCO-2. We confirmed that the explained variations in X_{H_2O} were primarily related to mesoscale transport using the tracer transport framework to compare temporal variability to spatial variations. For X_{H_2O}, observed explained spatial variations of X_{H_2O} were consistent with estimated explained variations within this framework (Fig. 8a and 8b).

In contrast, we were not able to fully characterize the variance budget for X_{CO_2}. Within our physical framework, the explained variations of X_{CO_2} observed by OCO-2 (Fig. 8c and 8e) were too large to be explained solely by mesoscale atmospheric transport. We note that this mismatch was particularly acute when using the geostatistically-estimated a_{space} from OCO-2 (around 20 km) for X_{CO_2}, but was also true when we substituted the observed a_{space} for X_{H_2O} (Fig. 8d). Together, these suggest another source of spatially coherent variance in OCO-2 X_{CO_2} that both shortens the length scale of coherence and contributes additional spatially coherent variability. Based on correlation analysis with other elements of the state vector, we conclude that high-pass filtered X_{CO_2} fields from v8 of the OCO-2 Level 2 X_{CO_2} retrieval

impart such structure and may explain part, though perhaps not all, of the mismatch in mesoscale time-space X_{CO_2} variability from TCCON and OCO-2. Correlations among elements of the retrieval state vector have also manifested in biases in X_{CO_2} retrieval output from GOSAT data, resulting in uncertainty of the magnitude and sign of posterior regional-scale flux estimates (Chevallier et al., 2014).

Our estimates of explained and unexplained variability can be compared against other studies that leverage the OCO-2 data set. For instance, Worden et al., (2017) analyzed the contribution of natural variations simulated by NASA's high resolution GEOS-5 simulation to the OCO-2 error budget. They found that the natural variability of X_{CO_2} within 100 km neighborhoods was only about 0.08 ppm, and that the observed variability from OCO-2 exceeded this value due to bias from other elements of the OCO-2 v7 retrieval vector. We used our framework to estimate the natural (or mesoscale) contribution to variations in X_{CO_2} with our space-for-time framework. Based on mesoscale variations at northern hemisphere TCCON stations, we expect that the imprint of mesoscale systems along the satellite track should be about 0.4 ppm (over 250 km). That our value is larger than the natural variability in model output reported by Worden et al. (2017) underscores the utility of our geostatistical approach for quantification of the variance budget based on observations themselves, rather than model output that may contain its own set of biases. Further, our methodology enables us to quantify the random error in the observations (unexplained variability) as well as the spatially coherent error (the portion of the explained variability caused by systematic bias in the retrieval).

Our results suggest that our analysis framework yields robust quantification of the influence of mesoscale transport for X_{H_2O}, despite the fact that local surface processes are likely also to impart local variations on this quantity. We acknowledge that our method to subtract local influence based on a climatological diurnal signal may result in biases of up to 30% of the fraction of variability in TCCON data being attributed to transport (Fig. 2). Ultimately, the methodology to account for local signals at TCCON sites would benefit from additional information on local fluxes across all sites, either from observations, such as eddy covariance fluxes, or from mechanistic coupled atmosphere-land models. Despite this caveat, the agreement between TCCON and X_{H_2O} variations suggests that the 250 km filter used and the assumptions made in this manuscript are sufficient to account for the structure imparted by fine spatial scale transport.

Although there were complications with X_{CO_2}, our results are promising for the use of geostatistical methods for parameterizing errors in inverse modeling frameworks. While we had hypothesized that our approach would allow us to separate the influence of mesoscale transport on X_{CO_2}, we note that for robust flux inference, proper accounting for spatially coherent non-transport structures within the data is also necessary. The approach presented in this study can be applied to each subsequent data release, and we anticipate that as the retrieval algorithm becomes more mature, the importance of correlated errors will decrease and the role of mesoscale transport will be revealed more clearly. Our results highlight the importance of continued development of the OCO-2 retrieval algorithm, since correlations between X_{CO_2} and other elements of the state vector may induce bias and spurious spatial correlation in X_{CO_2} that mask the influence of atmospheric transport.

Our results also highlight the importance of constraining variations of X_{CO_2} attributed to atmospheric transport for improved inferences of carbon fluxes from inversion models. While the influence of random errors can be minimized by averaging multiple soundings, transport-driven processes introduce variability on X_{CO_2} observations that are both spatially and temporally correlated. For example, taking a 10 s average of X_{CO_2} observations along the OCO-2 track (about 70 km), similar to the method presented in Crowell et al. (2019) will reduce the unexplained error (Fig. 6d) by $\frac{1}{\sqrt{N}}$ where N is the number of soundings in the averaging bin, because the unexplained errors for each sounding are assumed to be independent. In contrast the mean error for a bin decreases only by $\frac{1}{\sqrt{N_{effective}}}$ for the spatially correlated transport variability (Fig. 6e), where N$_{effective}$ can be approximated as the bin length divided by the geostatistical range (or autocorrelation length), which for X_{CO_2} is roughly 2-3 and may actually be closer to 1 if the X_{H_2O} ranges are used as more appropriate. Since the length-scales at which the resolved variability is correlated are comparable to the spatial distance encompassed by a 10-s along track average (Figure 7), the mesoscale variance is a key element of the signal that will be used in the inversions even when observations are aggregated. Given that the imprint of mesoscale and synoptic scale variance is not spatially or temporally uniform, ignoring it in an inverse modeling framework will lead to over confidence in some observational aggregates and underconfidence in others, ultimately shifting the distribution of fluxes. This is analogous to conducting a simple linear regression in which uniform error bars are assumed instead of assigning realistic errors to individual

points; the resulting slope and intercept will differ depending on the method of assigning errors. Inversion techniques typically require uncertainty estimates and their correlations on the inversion grid-scale, which spans from roughly mesoscale (~100km) to several times mesoscale depending on the transport model resolution. The appropriate uncertainty estimate will incorporate both instrument and algorithm error and spatially/temporally coherent subgrid-scale variability induced by transport and surface flux processes. Based on our analysis of both TCCON and OCO-2, the coherent mesoscale variability signal for X_{CO_2} is substantial relative to sounding errors alone and may be larger than transport variability estimates produced by most carbon cycle models, which may inadequately resolve mesoscale dynamics. Since mesoscale systems may have also been associated with frontal cloud coverage, lack of ability to constrain mesoscale variations may have resulted in large representation errors in inverse modeling (Corbin et al. 2008). Our results suggested that as a first step, we could use the explained variability derived from geostatistical analysis of OCO-2 data to inflate error estimates within inverse modeling systems. As a next step, we recommend the development of coupled high-resolution CO2-weather models that fully capture fine-to-large scale spatial and temporal variations in carbon fluxes, as an alternative to constrain the imprint of atmospheric transport from X_{CO_2} observations provided by OCO-2, OCO-3, and other emerging CO_2 monitoring satellites."

Acknowledgments

References

Baker, D. F., Law, R. M., Gurney, K. R., Rayner, P., Peylin, P., Denning, A. S., et al. (2006). TransCom 3 inversion intercomparison: Impact of transport model errors on the interannual variability of regional CO_2 fluxes, 1988-2003. *Global Biogeochemical Cycles*, *20*(1), GB1002. https://doi.org/10.1029/2004GB002439

Baker, D.F., H. Bösch, S.C. Doney, D. O'Brien, and D.S. Schimel, 2010: Carbon source/sink information provided by column CO_2 measurements from the Orbiting Carbon Observatory, *Atmosp. Chem. Physics,* *10*, 4145-4165. https://doi.org/10.5194/acp-10-4145-2010

Baldocchi, D., Falge, E., Gu, L., Olson, R., Hollinger, D., Running, S., … Wofsy, S. (2001). FLUXNET: A New Tool to Study the Temporal and Spatial Variability of Ecosystem–Scale Carbon Dioxide, Water Vapor, and Energy Flux Densities. *Bulletin of the American Meteorological Society, 82*(11), 2415–2434. https://doi.org/10.1175/1520-0477(2001)082<2415:fantts>2.3.co;2

Basu, S., Baker, D. F., Chevallier, F., Patra, P. K., Liu, J., & Miller, J. B. (2018). The impact of transport model differences on CO_2; surface flux estimates from OCO-2 retrievals of column average CO_2; *Atmospheric Chemistry and Physics*, *18*(10), 7189–7215. https://doi.org/10.5194/acp-18-7189-2018

Bolin, B., & Keeling, C. D. (1963). Large-scale atmospheric mixing as deduced from the seasonal and meridional variations of carbon dioxide. Journal of Geophysical Research, 68(13), 3899–3920. https://doi.org/10.1029/jz068i013p03899

Chevallier, F., Ciais, P., Conway, T. J., Aalto, T., Anderson, B. E., Bousquet, P., et al. (2010). CO_2 surface fluxes at grid point scale estimated from a global 21 year reanalysis of atmospheric measurements. *Journal of Geophysical Research*, *115*(D21), D21307. https://doi.org/10.1029/2010JD013887

Chevallier, F., & O'Dell, C. W. (2013). Error statistics of Bayesian CO_2 flux inversion schemes as seen from GOSAT. *Geophysical Research Letters*, *40*(6), 1252–1256. https://doi.org/10.1002/grl.50228

Chevallier, F., Palmer, P. I., Feng, L., Boesch, H., O'Dell, C. W., & Bousquet, P. (2014). Toward robust and consistent regional CO_2 flux estimates from in situ and spaceborne measurements of atmospheric CO_2. *Geophysical Research Letters*, *41*(3), 1065–1070. https://doi.org/10.1002/2013gl058772

Connor, B. J., Boesch, H., Toon, G., Sen, B., Miller, C., & Crisp, D. (2008). Orbiting Carbon Observatory: Inverse method and prospective error analysis. *Journal of Geophysical Research: Atmospheres*, *113*(D5), D05305. https://doi.org/10.1029/2006jd008336

Corbin, K. D., Denning, A. S., Lu, L., Wang, J.-W., & Baker, I. T. (2008). Possible representation errors in inversions of satellite CO_2 retrievals. *Journal of Geophysical Research*, *113*(D2), D02301. https://doi.org/10.1029/2007jd008716

Cressie, N., & Hawkins, D. M. (1980). Robust estimation of the variogram: I. *Journal of the International Association for Mathematical Geology*, *12*(2), 115–125. https://doi.org/10.1007/BF01035243

Crowell, S., Baker, D., Schuh, A., Basu, S., Jacobson, A. R., Chevallier, F., et al. (2019, in review). The 2015-2016 Carbon Cycle As Seen from OCO-2 and the Global *In Situ* Network. Atmospheric Chemistry and Physics Discussions, 1–79. https://doi.org/10.5194/acp-2019-87

Crisp, D., Atlas, R.., Breon, F.-M., Brown, L.., Burrows, J.., Ciais, P., et al. (2004). The Orbiting Carbon Observatory (OCO) mission. *Advances in Space Research*, *34*(4), 700–709. https://doi.org/10.1016/j.asr.2003.08.062

Dai, A., Wang, J., Ware, R. H., & Van Hove, T. (2002). Diurnal variation in water vapor over North America and its implications for sampling errors in radiosonde humidity. *Journal of Geophysical Research: Atmospheres*, *107*(D10), ACL 11-1-ACL 11-14. https://doi.org/10.1029/2001JD000642

De Mazière, M., Sha, M. K., Desmet, F., Hermans, C., Scolas, F., Kumps, N., et al. (2014). TCCON data from Reunion Island (La Reunion), France, Release GGG2014R0. https://doi.org/10.14291/tccon.ggg2014.reunion01.R0/1149288

Desai, A. (2016). AmeriFlux US-PFa Park Falls/WLEF [Data set]. AmeriFlux; University of Wisconsin. https://doi.org/10.17190/amf/1246090

Deutscher, N. M., Griffith, D. W. T., Bryant, G. W., Wennberg, P. O., Toon, G. C., Washenfelder, R. A., et al. (2010). Total column CO_2 measurements at Darwin, Australia – site description and calibration against in situ aircraft profiles. *Atmospheric Measurement Techniques*, 3(4), 947–958. https://doi.org/10.5194/amt-3-947-2010

Deutscher, N., Notholt, J., Messerschmidt, J., Weinzierl, C., Warneke, T., Petri, C., et al. (2014). TCCON data from Bialystok, Poland, Release GGG2014R1. https://doi.org/10.14291/tccon.ggg2014.bialystok01.R1/1183984

Eldering, A., O'Dell, C. W., Wennberg, P. O., Crisp, D., Gunson, M. R., Viatte, C., et al. (2017). The Orbiting Carbon Observatory-2: first 18 months of science data products. *Atmospheric Measurement Techniques*, *10*(2), 549–563. https://doi.org/10.5194/amt-10-549-2017

Enting, I. G., & Mansbridge, J. V. (1989). Seasonal sources and sinks of atmospheric CO_2: Direct inversion of filtered data. *Tellus B: Chemical and Physical Meteorology*, *41*(2), 111–126. https://doi.org/10.3402/tellusb.v41i2.15056

Geels, C., Doney, S. C., Dargaville, R., Brandt, J., & Christensen, J. H. (2004). Investigating the sources of synoptic variability in atmospheric CO2 measurements over the Northern Hemisphere continents: a

regional model study. Tellus B: Chemical and Physical Meteorology, 56(1), 35–50. https://doi.org/10.3402/tellusb.v56i1.16399

Glover, D. M., Jenkins, W. J., & Doney, S. C. (2011). Modeling Methods for Marine Science. Cambridge: Cambridge University Press. https://doi.org/10.1017/CBO9780511975721

Griffith, D. W. T., Deutscher, N., Velazco, V. A., Wennberg, P. O., Yavin, Y., Aleks, G. K., et al. (2014). TCCON data from Darwin, Australia, Release GGG2014R0. https://doi.org/10.14291/tccon.ggg2014.darwin01.R0/1149290

Gurney, K. R., Law, R. M., Denning, A. S., Rayner, P. J., Baker, D., Bousquet, P., et al. (2002). Towards robust regional estimates of CO2 sources and sinks using atmospheric transport models. *Nature*, *415*(6872), 626–630. https://doi.org/10.1038/415626a

Hase, F., Blumenstock, T., Dohe, S., Gross, J., & Kiel, M. (2014). TCCON data from Karlsruhe, Germany, Release GGG2014R1. https://doi.org/10.14291/tccon.ggg2014.karlsruhe01.R1/1182416

Houweling, S., Baker, D., Basu, S., Boesch, H., Butz, A., Chevallier, F., et al. (2015). An intercomparison of inverse models for estimating sources and sinks of CO_2 using GOSAT measurements. *Journal of Geophysical Research: Atmospheres*, *120*(10), 5253–5266. https://doi.org/10.1002/2014JD022962

Keeling, R. F., Piper, S. C., & Heimann, M. (1996). Global and hemispheric CO_2 sinks deduced from changes in atmospheric O2 concentration. *Nature*, *381*(6579), 218–221. https://doi.org/10.1038/381218a0

Keppel-Aleks, G., Wennberg, P. O., & Schneider, T. (2011). Sources of variations in total column carbon dioxide. *Atmospheric Chemistry and Physics*, *11*(8), 3581–3593. https://doi.org/10.5194/acp-11-3581-2011

Keppel-Aleks, G., Wennberg, P. O., Washenfelder, R. A., Wunch, D., Schneider, T., Toon, G. C., et al. (2012). The imprint of surface fluxes and transport on variations in total column carbon dioxide. *Biogeosciences*, *9*(3), 875–891. https://doi.org/10.5194/bg-9-875-2012

Landschützer, P., Gruber, N., Haumann, F. A., Rödenbeck, C., Bakker, D. C. E., van Heuven, S., et al. (2015). The reinvigoration of the Southern Ocean carbon sink. *Science*, *349*(6253), 1221–1224. https://doi.org/10.1126/science.aab2620

Masarie, K. A., Pétron, G., Andrews, A., Bruhwiler, L., Conway, T. J., Jacobson, A. R., et al. (2011). Impact of CO2 measurement bias on CarbonTracker surface flux estimates. *Journal of Geophysical Research*, *116*(D17), D17305. https://doi.org/10.1029/2011JD016270

Mesinger, F., DiMego, G., Kalnay, E., Mitchell, K., Shafran, P. C., Ebisuzaki, W., et al. (2006). North American Regional Reanalysis. Bulletin of the American Meteorological Society, 87(3), 343–360. https://doi.org/10.1175/bams-87-3-343

Miller, C. E., Crisp, D., DeCola, P. L., Olsen, S. C., Randerson, J. T., Michalak, A. M., et al. (2007). Precision requirements for space-based data. *Journal of Geophysical Research: Atmospheres*, *112*(D10), D10314. https://doi.org/10.1029/2006JD007659

Miller, S. M., Hayek, M. N., Andrews, A. E., Fung, I., & Liu, J. (2015). Biases in atmospheric CO_2; estimates from correlated meteorology modeling errors. Atmospheric Chemistry and Physics, 15(5), 2903–2914. https://doi.org/10.5194/acp-15-2903-2015

Miller, S. M., Michalak, A. M., Yadav, V., & Tadić, J. M. (2018). Characterizing biospheric carbon balance using CO_2; observations from the OCO-2 satellite. Atmospheric Chemistry and Physics, 18(9), 6785–6799. https://doi.org/10.5194/acp-18-6785-2018

Nelson, R. R., Crisp, D., Ott, L. E., & O'Dell, C. W. (2016). High-accuracy measurements of total column water vapor from the Orbiting Carbon Observatory-2. *Geophysical Research Letters*, *43*(23), 12,212-261,269. https://doi.org/10.1002/2016gl071200

O'Dell, C. W., Connor, B., Bösch, H., O'Brien, D., Frankenberg, C., Castano, R., et al. (2012). The ACOS CO_2 retrieval algorithm-Part 1: Description and validation against synthetic observations. *Atmospheric Measurement Techniques*, *5*(1), 99–121. https://doi.org/10.5194/amt-5-99-2012

O'Dell, C. W., Eldering, A., Wennberg, P. O., Crisp, D., Gunson, M. R., Fisher, B., et al. (2018). Improved Retrievals of Carbon Dioxide from the Orbiting Carbon Observatory-2 with the version 8 ACOS algorithm. *Atmospheric Measurement Techniques Discussions*, 1–57. https://doi.org/10.5194/amt-2018-257

Olsen, S. C., and J. T. Randerson (2004), Differences between surface and column atmospheric CO2 and implications for carbon cycle research, *J. Geophys. Res.*, *109*, D02301. https://doi.org/10.1029/2003JD003968

Parazoo, N. C., Denning, A. S., Kawa, S. R., Corbin, K. D., Lokupitiya, R. S., & Baker, I. T. (2008). Mechanisms for synoptic variations of atmospheric CO_2 in North America, South America and Europe. *Atmospheric Chemistry and Physics*, *8*(23), 7239–7254. https://doi.org/10.5194/acp-8-7239-2008

Parazoo, N. C., Denning, A. S., Berry, J. A., Wolf, A., Randall, D. A., Kawa, S. R., et al. (2011). Moist synoptic transport of CO_2 along the mid-latitude storm track. *Geophysical Research Letters*, *38*(9), L09804. https://doi.org/10.1029/2011gl047238

Peters, W., Miller, J. B., Whitaker, J., Denning, A. S., Hirsch, A., Krol, M. C., et al. (2005). An ensemble data assimilation system to estimate CO_2 surface fluxes from atmospheric trace gas observations. *Journal of Geophysical Research*, *110*(D24), D24304. https://doi.org/10.1029/2005jd006157

Peters, W., Jacobson, A. R., Sweeney, C., Andrews, A. E., Conway, T. J., Masarie, K., et al. (2007). An atmospheric perspective on North American carbon dioxide exchange: {CarbonTracker}. *Proceedings of the National Academy of Sciences*, *104*(48), 18925–18930. https://doi.org/10.1073/pnas.0708986104

Peylin, P., Law, R. M., Gurney, K. R., Chevallier, F., Jacobson, A. R., Maki, T., et al. (2013). Global atmospheric carbon budget: Results from an ensemble of atmospheric CO2 inversions. *Biogeosciences*, *10*(10), 6699–6720. https://doi.org/10.5194/bg-10-6699-2013

Rayner, P. J., & O'Brien, D. M. (2001). The utility of remotely sensed CO_2 concentration data in surface source inversions. *Geophysical Research Letters*, *28*(1), 175–178. https://doi.org/10.1029/2000gl011912

Rodgers, C. D. (2000). Inverse Methods for Atmospheric Sounding: Theory and Practice. Singapore: World Scientific. https://doi.org/10.1142/9789812813718_0001

Ross, A. N., Wooster, M. J., Boesch, H., & Parker, R. (2013). First satellite measurements of carbon dioxide and methane emission ratios in wildfire plumes. *Geophysical Research Letters*, *40*(15), 4098–4102. https://doi.org/10.1002/grl.50733

Sherlock, V., Connor, B., Robinson, J., Shiona, H., Smale, D., & Pollard, D. (2014). TCCON data from Lauder, New Zealand, 120HR, Release GGG2014R0. https://doi.org/10.14291/tccon.ggg2014.lauder01.R0/1149293

Stephens, B. B., Gurney, K. R., Tans, P. P., Sweeney, C., Peters, W., Bruhwiler, L., et al. (2007). Weak Northern and Strong Tropical Land Carbon Uptake from Vertical Profiles of Atmospheric CO_2. *Science*, *316*(5832), 1732–1735. https://doi.org/10.1126/science.1137004

Sussmann, R., & Rettinger, M. (2014). TCCON data from Garmisch, Germany, Release GGG2014R0. https://doi.org/10.14291/tccon.ggg2014.garmisch01.R0/1149299

Tans, P. P., Fung, I. Y., & Takahashi, T. (1990). Observational Contrains on the Global Atmospheric CO_2 Budget. *Science*, *247*(4949), 1431–1438. https://doi.org/10.1126/science.247.4949.1431

Tans, P. P., & Keeling, C. D. (2017). Atmospheric Monthly In Situ CO2 Data - Mauna Loa Observatory, Hawaii. In Scripps CO2 Program Data [Data set]. UC San Diego Library Digital Collections. https://doi.org/10.6075/j08w3bhw

Warneke, T., Messerschmidt, J., Notholt, J., Weinzierl, C., Deutscher, N., Petri, C., et al. (2014). TCCON data from Orleans, France, Release GGG2014R0. https://doi.org/10.14291/tccon.ggg2014.orleans01.R0/1149276

Washenfelder, R. A., Toon, G. C., Blavier, J.-F., Yang, Z., Allen, N. T., Wennberg, P. O., et al. (2006). Carbon dioxide column abundances at the Wisconsin Tall Tower site. *Journal of Geophysical Research*, *111*(D22), D22305. https://doi.org/10.1029/2006jd007154

Wennberg, P. O., Roehl, C., Wunch, D., Toon, G. C., Blavier, J.-F., Washenfelder, R., et al. (2014). TCCON data from Park Falls, Wisconsin, USA, Release GGG2014R0. https://doi.org/10.14291/tccon.ggg2014.parkfalls01.R0/1149161

Wennberg, P. O., Wunch, D., Roehl, C., Blavier, J.-F., Toon, G. C., Allen, N., et al. (2014). TCCON data from Lamont, Oklahoma, USA, Release GGG2014R0. https://doi.org/10.14291/tccon.ggg2014.lamont01.R0/1149159

Williams, I. N., Riley, W. J., Torn, M. S., Biraud, S. C., & Fischer, M. L. (2014). Biases in regional carbon budgets from covariation of surface fluxes and weather in transport model inversions. *Atmospheric Chemistry and Physics*, *14*(3), 1571–1585. https://doi.org/10.5194/acp-14-1571-2014

Wofsy, S. C. (2011). HIAPER Pole-to-Pole Observations (HIPPO): fine-grained, global-scale measurements of climatically important atmospheric gases and aerosols. *Philosophical Transactions of the Royal Society A: Mathematical, Physical and Engineering Sciences*, *369*(1943), 2073–2086. https://doi.org/10.1098/rsta.2010.0313

Wofsy, S., Daube, B., Jimenez, R., Kort, E., Pittman, J., Park, S., et al. (2017). HIPPO Pressure-Weighted Mean Total, 10-km, and 100-m Interval Column Concentrations. Version 1.0 (Data set). UCAR/NCAR - Earth Observing Laboratory. https://doi.org/10.3334/cdiac/hippo_011. Accessed 03 Mar 2018.

Worden, R. J., Doran, G., Kulawik, S., Eldering, A., Crisp, D., Frankenberg, C., et al. (2017). Evaluation and attribution of OCO-2 X_{CO_2} uncertainties. *Atmospheric Measurement Techniques*, *10*(7), 2759–2771. https://doi.org/10.5194/amt-10-2759-2017

Wunch, D., Toon, G. C., Wennberg, P. O., Wofsy, S. C., Stephens, B. B., Fischer, M. L., et al. (2010). Calibration of the Total Carbon Column Observing Network using aircraft profile data. *Atmospheric Measurement Techniques*, *3*(5), 1351–1362. https://doi.org/10.5194/amt-3-1351-2010

Wunch, D., Toon, G. C., Blavier, J.-F. L., Washenfelder, R. A., Notholt, J., Connor, B. J., et al. (2011). The Total Carbon Column Observing Network. *Philosophical Transactions of the Royal Society A: Mathematical, Physical and Engineering Sciences*, *369*(1943), 2087–2112. https://doi.org/10.1098/rsta.2010.0240

Wunch, D., Toon, G. C., Sherlock, V., Deutscher, N. M., Liu, C., Feist, D. G., & Wennberg, P. O. (2015). *The Total Carbon Column Observing Network's GGG2014 Data Version*. Carbon Dioxide Information Analysis Center, Oak Ridge National Laboratory, Oak Ridge, Tennessee, U.S.A. https://doi.org/10.14291/tccon.ggg2014.documentation. R0/1221662

Wunch, D., P. O. Wennberg, G. B. Osterman, B. Fisher, B. Naylor, C. M. Roehl, C. O'Dell, L. Mandrake, C. Viatte, M. Kiel, D. W. T. Griffith, N. M. Deutscher, V. A. Velazco, J. Notholt, T. Warneke, C. Petri, M. De Maziere, M. K. Sha, R. Sussmann, M. Rettinger, D. Pollard, J. Robinson, I. Morino, O. Uchino, F. Hase, T. Blumenstock, D. G. Feist, S. G. Arnold, K. Strong, J. Mendonca, R. Kivi, P. Heikkinen, L. Iraci, J. Podolske, P. W. Hillyard, S. Kawakami, M. K. Dubey, H. A. Parker, E. Sepulveda, O. E. Garc?a, Y. Te, P. Jeseck, M. R. Gunson, D. Crisp, and A. Eldering (2017), Comparisons of the Orbiting Carbon Observatory-2 (OCO-2) X_{CO_2} measurements with TCCON, Atmos. Meas. Tech., 10(6), 2209–2238, doi:10.5194/amt-10-2209-2017.

Yang, D., Liu, Y., Cai, Z., Chen, X., Yao, L., & Lu, D. (2018). First Global Carbon Dioxide Maps Produced from TanSat Measurements. Advances in Atmospheric Sciences, 35(6), 621–623. https://doi.org/10.1007/s00376-018-7312-6

Yokota, T., Yoshida, Y., Eguchi, N., Ota, Y., Tanaka, T., Watanabe, H., & Maksyutov, S. (2009). Global Concentrations of CO_2 and CH_4 Retrieved from GOSAT: First Preliminary Results. *SOLA*, *5*, 160–163. https://doi.org/10.2151/sola.2009-041